Tunneling spectroscopy with intrinsic Josephson junctions in $Bi_2Sr_2CaCu_2O_{8+\delta}$ and $Tl_2Ba_2Ca_2Cu_3O_{10+\delta}$

K. Schlenga,* R. Kleiner, G. Hechtfischer, M. Mößle, S. Schmitt, and Paul Müller
Physikalisches Institut III, Universität Erlangen–Nürnberg, D-91058 Erlangen, Germany

Ch. Helm, Ch. Preis, F. Forsthofer, and J. Keller
Institut für Theoretische Physik, Universität Regensburg, D-93040 Regensburg, Germany

H. L. Johnson
Commonwealth Scientific and Industrial Research Organisation (CSIRO), Telecommunications and Industrial Physics, Lindfield 2070, Australia

M. Veith and E. Steinbeiß
Institut für Physikalische Hochtechnologie (IPHT) Jena, D-07743 Jena, Germany
(Received 16 October 1997)

The paper presents a detailed discussion of the current-voltage characteristic of intrinsic Josephson junctions in $Bi_2Sr_2CaCu_2O_{8+\delta}$ and $Tl_2Ba_2Ca_2Cu_3O_{10+\delta}$. In these materials Josephson tunnel junctions are formed naturally between adjacent superconducting CuO_2 bilayers or trilayers. A typical sample consists of a stack of Josephson junctions. We explicitly show that all junctions inside a given sample have identical tunneling characteristics. We discuss the shape (general curvature) of the current-voltage characteristic in terms of a superconducting order parameter that has a predominant $d_{x^2-y^2}$ symmetry. The I_cR_n product of the intrinsic Josephson junctions turns out to be 2–3 mV, about 10% of the maximum energy gap Δ_0/e. The current-voltage characteristic of every individual junction exhibits pronounced structures in the subgap regime. They are best explained by a recently proposed resonant coupling mechanism between infrared active optical c-axis phonons and oscillating Josephson currents. [S0163-1829(98)00221-5]

I. INTRODUCTION

The high transition temperature (T_c) superconductors form natural superconducting multilayers where the superconducting order parameter is periodically modulated along the c axis (perpendicular to the CuO_2 layers). At least in highly anisotropic compounds such as $Bi_2Sr_2CaCu_2O_{8+\delta}$ (BSCCO) or $Tl_2Ba_2Ca_2Cu_3O_{10+\delta}$ (TBCCO), the modulation is strong enough that adjacent superconducting copper oxide double or triple layers are only weakly coupled by the Josephson effect. This behavior can be directly observed in c-axis transport measurements in sufficiently small samples.[1–16] Every pair of adjacent copper oxide double or triple planes, together with the intervening nonsuperconducting layers, forms an intrinsic Josephson junction, i.e., the whole crystal acts as a vertical stack of junctions. The experimental proof of intrinsic Josephson effects[1] included investigations of the supercurrent as a function of magnetic field and temperature, Shapiro steps, and Josephson microwave emission. This provided a good understanding of the c-axis supercurrents. In contrast, the dielectric properties of the intrinsic junctions and the physics of the quasiparticle current, which is intimately connected with the quasiparticle density of states, are not well understood. As the superconducting order parameter in BSCCO and TBCCO is known to have predominantly $d_{x^2-y^2}$ symmetry,[17–22] intrinsic Josephson junctions should be considered as c-axis tunnel junctions between two $d_{x^2-y^2}$ superconductors. It is of interest to test to what extent experimental data are consistent with this picture. A crucial question is whether standard tunneling formalism (see, e.g., Ref. 23) can be applied to quasiparticle tunneling between two adjacent superconducting multilayers.

An important quantity for the characterization of Josephson tunnel junctions is the product of critical current I_c and normal state resistance R_n. For conventional tunnel junctions $I_cR_n = \pi\Delta/2e$ (Ref. 24) (Δ being the energy gap). For a c-axis Josephson tunnel junction between two $d_{x^2-y^2}$ superconductors, I_cR_n has been calculated to be Δ/e or smaller.[25] Experimental data for comparison, however, are still lacking.

The current-voltage (I-V) characteristics of tunnel junctions between conventional superconductors contain information about microscopic properties of the material.[26,27] In high-T_c superconductors it is extremely difficult to fabricate tunnel junctions with well-controlled properties. A number of preparation techniques have been reported that produce high quality junctions in BSCCO, for example, vacuum tunneling spectroscopy,[28–31] point contact spectroscopy,[32–36] planar junction geometries,[37–39] or break junctions.[40,41] However, tunneling experiments with such artificial tunnel structures effectively probe only the outermost few angstroms of the sample. Due to the short coherence length, any surface roughness or surface degradation even on an atomic scale obscures intrinsic properties. In contrast, measurements of the properties of intrinsic Josephson junctions are insensitive to surface degradation and are able to probe the bulk of a sample layer by layer. A close investigation of structures on the quasiparticle branch of the I-V characteristic should,

therefore, provide insight into the bulk properties of the material that would otherwise be inaccessible.

The above considerations assume that the *I-V* characteristic of individual junctions in the stack is at most weakly influenced by the presence of the other junctions. Adjacent junctions can be inductively coupled by supercurrents flowing along the superconducting layers.[42,7,8] This effect occurs in large magnetic fields oriented parallel to the layers. On the *I-V* characteristic it leads to an additional voltage drop, which is due to a (collective) motion of Josephson vortices. The quasiparticle branch of individual junctions, however, remains unaffected. Moreover, in zero magnetic field and for transport currents flowing perpendicular to the layers, screening currents and thus inductive coupling are negligibly small. Another kind of coupling that is currently under investigation[43,44] may arise from the modification of the chemical potentials of the superconducting layers due to the tunneling of Cooper pairs. Its impact on the *I-V* characteristic is currently unclear. However, we will show that the effect seems to be small at least for the geometries discussed in this paper. The main features of the *I-V* characteristic of the stack can be understood best if one assumes that the junctions are independent. We discuss the *c*-axis *I-V* characteristics of BSCCO and TBCCO samples. Since the experimental data for BSCCO and TBCCO are qualitatively similar, we will not always show the results for both compounds. The paper is organized as follows. Section II presents sample preparation and measurement techniques. In Sec. III we show that the intrinsic junctions located in a given crystal all exhibit identical tunneling characteristics. We then compare the tunneling characteristics of different samples to demonstrate reproducibility. Differences seem to depend only on the carrier concentration and critical temperature. Finally, we compare the experimental data to a theoretical tunneling characteristic and determine the I_cR_n product. Section IV is devoted to the recently reported subgap structures in the *I-V* characteristics of both materials.

II. EXPERIMENTS

Measurements of the *I-V* characteristics with the transport current in the *c* direction have been performed with mesa structures patterned on the surface of BSCCO single crystals[11] and with step stacks fabricated on thin TBCCO films.[2,6]

The BSCCO crystals were grown in an oxygen atmosphere by the floating zone technique.[45] X-ray diffraction confirms that the crystals are single phase Bi(2212), and energy dispersive x-ray analysis indicates a cation stoichiometry of approximately Bi:Sr:Ca:Cu = 2.2:1.8:1.1:2.[46] Using either standard photolithography and Ar-ion etching or chemical wet etching in a HNO_3 dilution (1:200), mesas of 16×16 μm^2 up to 40×40 μm^2 across and of varying heights between 150 nm and 1200 nm were fabricated on the *a-b* face of the crystal. BSCCO samples were measured in a two-terminal configuration with low resistance gold contacts sputtered onto the freshly cleaved *a-b* faces of the crystals [Fig. 1(a)]. The two-terminal configuration results in contact-resistance in the *I-V* data, which has been subtracted for data evaluation.

The step stacks are made on TBCCO thin films deposited

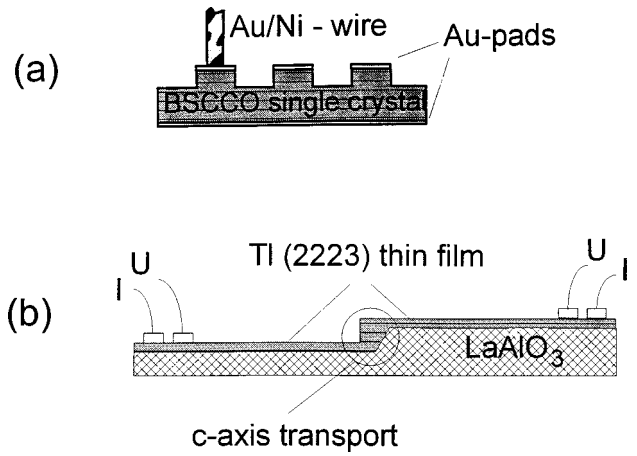

FIG. 1. (a) Sketch of $Bi_2Sr_2CaCu_2O_{8+\delta}$ single crystal mesas. Mesa cross section varies between 16×16 μm^2 and 40×40 μm^2. (b) Vertically structured Tl films (step stacks). Current flow in the circled region is perpendicular to the layers. The width of the microbridge at the step varies between 5 μm and 24 μm. Dimensions are not to scale.

on $LaAlO_3$ substrates with pre-etched step edges. For the film deposition, a precursor–post-anneal technique was used.[47] The T_c of the Tl(2223) films was as high as 115 K. For the preparation of intrinsic Josephson junctions, step edges were patterned into (100)$LaAlO_3$ substrates by ion beam etching. These steps had heights of 400–500 nm and slope angles between 60° and 75°. In contrast to $YBa_2CuO_{7-\delta}$ step edge junctions, the very fast lateral spreading of the Tl(2223) crystallites during film recrystallization[6] leads to a platelike overgrowth at the substrate step without a change in orientation. Choosing the substrate step to be higher than the film thickness leads to the desired perpendicular current flow across the substrate step [Fig. 1(b)]. After film deposition, microbridges of widths between 3 μm and 24 μm were patterned into the samples across the step, thus defining a stack of typically 100–200 intrinsic junctions at the step.[2,6] Transport measurements were made in a four-terminal configuration using indium pressure contacts directly onto the TBCCO film.

To reduce the influence of external noise, low-pass filters were used in the current and voltage leads. Some of the measurements were performed in a shielded room. The differential resistance dV/dI of the *I-V* characteristic was measured using a superimposed ac current and standard lock-in technique. Experimental details of the microwave experiments are described in Ref. 1. The measurements in external magnetic fields were performed in a horizontal split coil allowing *in situ* orientation as described in Ref. 7. The orientation accuracy is better than 1°.

III. GENERAL *I-V* CHARACTERISTIC

The *I-V* characteristic of an intrinsic junction stack exhibits a superconducting branch and a large number of branches in the resistive state. This structure can be explained by assuming that the *I-V* characteristic of every individual junction exhibits a superconducting and a resistive branch, similar to the *I-V* characteristic of standard Josephson tunnel junctions.[1] If all junctions of an *N* junction stack can be

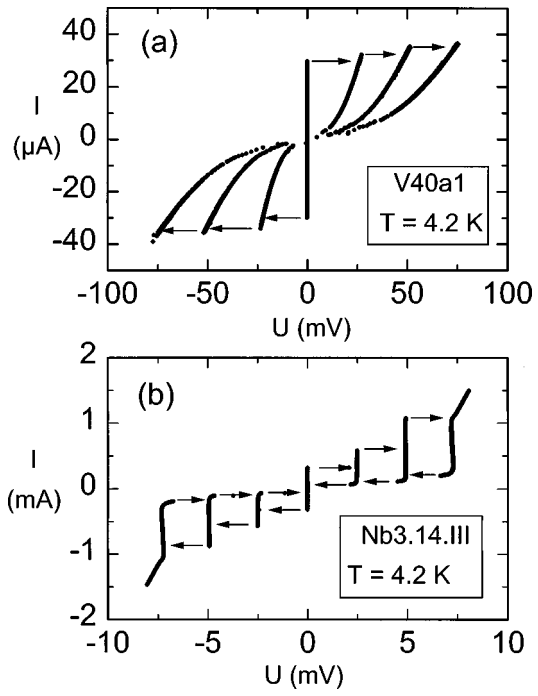

FIG. 2. (a) First three branches of the *I-V* characteristic of a $Tl_2Ba_2Ca_2Cu_3O_{10+\delta}$ step stack with a total number of 130 junctions; (b) *I-V* characteristics of an artificial three-junction Nb/Al-AlO_x/Nb stack. Arrows indicate voltage switching.

switched into the resistive state individually, the total *I-V* characteristic consists of $N+1$ branches differing by the number of junctions in the resistive state.[1] As an example, Fig. 2 shows (a) the first three branches of the *I-V* characteristic of an intrinsic junction stack (TBCCO step stack with a total number of 130 junctions) and for comparison (b) the complete *I-V* characteristic of an artificial threefold Nb Josephson junction stack, both at $T=4.2$ K. The complete *I-V* characteristic of the step stack sample is shown in Refs. 2 and 6, where the existence of 130 branches in the resistive state has been confirmed. After exceeding the critical current of an individual junction in the stack, the *I-V* characteristic exhibits a characteristic voltage jump V_c. For the Nb tunnel junctions, the jump is 2.5 mV for each junction. This is about $2\Delta/e$, the value expected for a standard SIS (superconductor-insulator-superconductor) tunnel junction. The voltage jump is approximately 27 mV in the TBCCO step stacks, and about 22 mV in BSCCO mesas. This value corresponds to roughly 50% of $2\Delta/e$.[28–41] The quasiparticle branch of the Nb tunnel junctions exhibits a nearly vertical current rise at the gap voltage $2\Delta/e$. In contrast, the characteristics of the intrinsic junctions show a gradual current rise.

If the junctions in the stack are essentially equal and independent, then at fixed bias current the voltage in the nth branch should simply be n times the voltage of the first branch, at least in the first few branches. In branches of higher order (with high voltages and currents), heating effects could affect the quasiparticle characteristic.[13] This is indeed the case, as we explicitly show in Fig. 3 by comparing the first three branches of the *I-V* characteristic. The voltages on the second and third branches have been scaled by a factor of 2 and 3, respectively, for comparison with the first branch. The three curves are identical, showing that

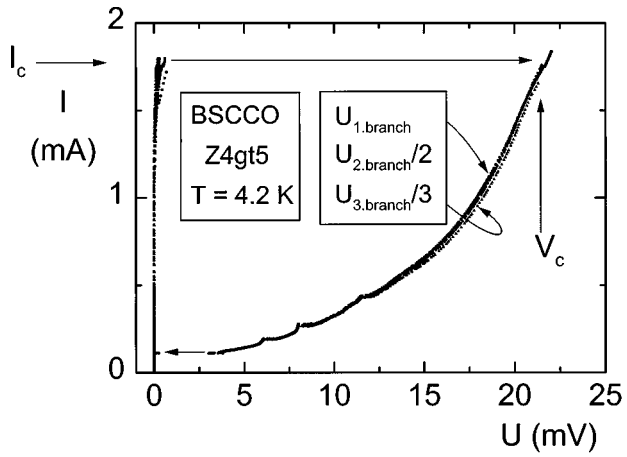

FIG. 3. Comparison of the first three branches of the *I-V* characteristic of a BSCCO mesa. The voltages of the second (third) branch have been divided by two (three).

these junctions have the same tunneling characteristics.

Recently, Machida *et al.* proposed an alternative explanation for the appearance of the multiple valued *I-V* characteristic.[43] It is claimed that the multiple branching is a consequence of different collective longitudinal Josephson plasma modes. For a given mode the total voltage across the stack would not be equally distributed among all junctions in the resistive state, and also the different branches in the *I-V* characteristic would not be separated equidistantly.[43,48] This is in contrast to our observations (cf. Fig. 3). The existence and the behavior of modes with well localized resistive regions in the model proposed by Ref. 43 will be investigated in a forthcoming publication.[44,49] From our measurements we conclude that the number of resistive junctions is not important for determining the shape of the quasiparticle *I-V* characteristic. It is thus justified to consider the characteristic of the first branch as being representative of all the junctions in the stack. The equidistant spacing of the branches and their curvature can then be explained by quasiparticle tunneling in the intrinsic Josephson junctions similar to the multiple valued *I-V* characteristic of a conventional Nb-Josephson junction stack [Fig. 2(b)], where the coupling due to modifications of the chemical potentials certainly plays no role. Note that with the assumption of independent junctions, the location of resistive junctions relative to other resistive junctions is completely undetermined. To what extend residual interactions change this picture is presently unclear.

A. *I-V* characteristic of individual junctions

As shown above, the resistive branches of different junctions in a given sample are identical. In addition, junctions in different BSCCO samples show nearly identical *I-V* characteristics. The curvature of the quasiparticle branch is seen in all intrinsic junctions and can be changed only slightly by doping. The first branch of the *I-V* characteristic of five different BSCCO mesa samples [see Fig. 4(a)] clearly shows an exponential dependence of the form

$$I=I_0\exp\left(\frac{V}{V_0}\right). \tag{1}$$

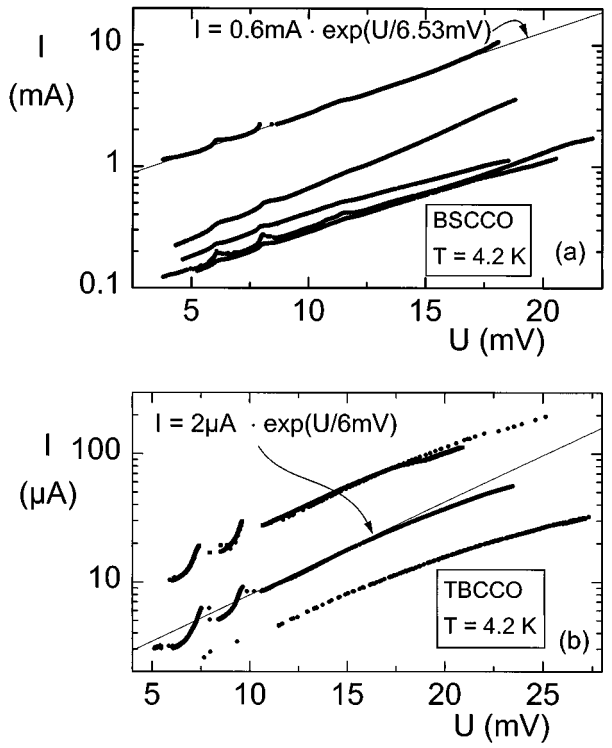

FIG. 4. Low temperature scaling behavior of intrinsic I-V characteristics of (a) different $Bi_2Sr_2CaCu_2O_{8+\delta}$ mesa samples and (b) different $Tl_2Ba_2Ca_2Cu_3O_{10+\delta}$ step stack samples. In (a) the first branch of the I-V characteristics of samples Z4gt5b, Z4gt5, Z4gt5c, D6*, and D7* (from bottom to top) is plotted. For sample D7* a fit to Eq. (1) is displayed. In (b) the first branch of samples V40a1, V91c1, and V40a34 (from bottom to top) is plotted. For sample V91c1, a fit to Eq. (1) is displayed.

The prefactor I_0 depends mainly on the junction size. The extracted values V_0 for the different samples are listed in Table I together with the critical temperatures. A relationship between these two quantities would be interesting but many more samples need to be investigated for this purpose.

The I-V characteristics of TBCCO step stack samples appear similar to the I-V characteristics of the BSCCO mesa samples. Figure 4(b) shows the first resistive branch of three different TBCCO step stack samples. The solid line represents an exponential fit to Eq. (1) for one of the TBCCO samples. Significant differences between fit and experimental data can be seen. For TBCCO, the experimentally observed I-V characteristics were not consistent with either an exponential dependence or a power law dependence (not shown).

TABLE I. BSCCO mesa samples, transition temperatures T_c, parameters V_0 derived with Eq. (1), critical currents I_c, normal state resistances R_n as determined from a fit according to Eq. (2) with $\Delta_0 = 25$ meV, and I_cR_n products.

Sample	T_c (K)	V_0 (mV)	I_c (mA)	R_n (Ω)	I_cR_n (mV)
D6*	80	5.22	3.54	0.56	2.0
Z4gt5c	86	6.1	0.925	1.67	1.5
Z4gt5b	86	6.76	1.23	2.2	2.7
Z4gt5	86	6.73	1.71	1.85	3.1
D7*	87	6.53	10.6	0.17	1.8

In the resistively shunted junction (RSJ) model[50] the current through a Josephson junction is given as the sum of the supercurrent I_s, the quasiparticle current I_{qp}, and the displacement current I_d. In junctions with a highly hysteretic I-V characteristic, as observed here, the resistive branch of the I-V characteristic is completely dominated by the quasiparticle current.[51] The other two channels cause only minor deviations from the pure quasiparticle characteristic. As a consequence, the explanation of the general curvature is reduced to that of the quasiparticle tunneling characteristic.

At low temperatures the tunneling characteristic of the intrinsic Josephson junctions in BSCCO as well as in TBCCO shows a high conductivity in the subgap regime ($V \ll 2\Delta/e \approx 50$ mV). This is in contrast to a pure BCS-like density of states, which leads to a steep current rise in the tunneling characteristic at a voltage $2\Delta/e$. In order to compare our results to theory, the tunneling quasiparticle current $I(V)$ was calculated using the expression

$$I = \frac{1}{eR_n} \int_{-\infty}^{\infty} N(E)N(E+eV)[f(E)-f(E+eV)]dE \tag{2}$$

given in Ref. 23. Here, R_n is the normal state resistance, $f(E)$ the distribution function, and $N(E)$ the normalized density of states of the superconductors. Because of the extremely small volume in the superconducting layers, it can be argued that the quasiparticle tunneling current introduces a significant nonequilibrium distribution in these layers. This might cause deviations from the equilibrium I-V characteristic and has been observed in artificial double-barrier tunnel junctions (see, for example, Ref. 52). However, as a starting point we will calculate the tunneling current with the Fermi function for $f(E)$. Both experiments probing the quasiparticle excitation spectrum[17–19] as well as phase sensitive experiments[20–22] provide increasing evidence that the order parameter in high-T_c superconductors has $d_{x^2-y^2}$ symmetry. Thus for the normalized density of states $N(E)$ we used the simplified expression for $d_{x^2-y^2}$-wave superconductors,[53]

$$N(E) = \mathrm{Re} \int_0^{2\pi} \frac{1}{2\pi} \left\{ \frac{E}{\sqrt{E^2-[\Delta_0 \cos(2\varphi)]^2}} \right\} d\varphi, \tag{3}$$

where φ is the in-plane angle in k space. The normalized d-wave density of states was evaluated via[53]

$$N(E) = \begin{cases} \dfrac{2}{\pi} \dfrac{E}{\Delta_0} K\left(\dfrac{E}{\Delta_0}\right), & |E| \leqslant \Delta_0 \\ \dfrac{2}{\pi} K\left(\dfrac{\Delta_0}{E}\right), & |E| > \Delta_0 \end{cases} \tag{4}$$

with the complete elliptic integral $K(x)$. We take $\Delta_0 = 25$ meV, a value that represents the mean of published results.[28–38,40,41] The tunneling current calculated from Eq. (2) is shown in Fig. 5(a). We also included the measured I-V characteristic of BSCCO sample Z4gt5. Note that the measured data are at bias currents below 2 mA. An enlargement of this region is shown in Fig. 5(b) and will be discussed below. At low voltages $V \ll \Delta_0/e$ the theoretical I-V characteristic follows a power law.[53] At the gap voltage $2\Delta_0/e$ there is a transition to a linear dependence. The asymptotic

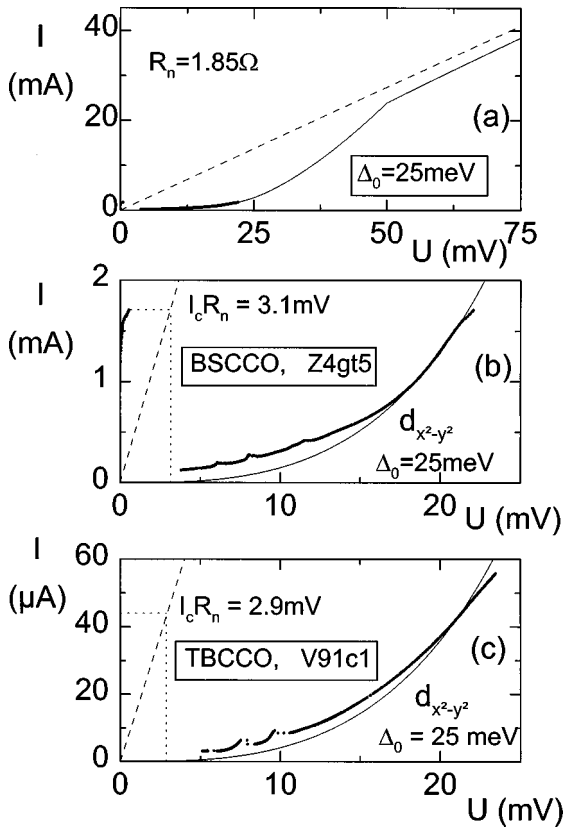

FIG. 5. (a) Calculated quasiparticle tunneling current for a junction between two *d*-wave superconductors (solid line) compared to measured data of an intrinsic BSCCO junction (symbols), and (b) the same data on an expanded scale. For the calculation, a gap parameter $\Delta_0 = 25$ meV was used. The dashed line indicates the asymptotic normal state resistance $R_n = 1.85\ \Omega$. The I_cR_n product is determined to be about 3.1 mV. (c) Comparison of the calculated tunneling characteristic (solid line, $\Delta_0 = 25$ meV, $R_n = 66.7\ \Omega$) to a measured *I-V* characteristic of an intrinsic TBCCO junction (symbols). The I_cR_n product is determined to be about 2.9 mV.

normal state resistance R_n is illustrated by the dashed line. It should be noted that if the order parameter has a mixed symmetry (e.g., $d+is$) with a clearly predominant $d_{x^2-y^2}$ part, the quasiparticle tunneling characteristic is dominated by the $d_{x^2-y^2}$ part. Thus the presence of a small *s*-wave component as observed by several authors[39,54–58] can be neglected for our purpose.

The comparison between the calculated tunneling characteristic at low currents and the experimental data of a single intrinsic Josephson junction in BSCCO is presented in Fig. 5(b). A reasonable agreement is achieved with $\Delta_0 = 25$ meV and $R_n = 1.85\ \Omega$. The excess current at low voltages in the measured *I-V* characteristic might partially arise from a contribution of rectified ac Josephson currents. As mentioned above, the calculated curve follows a power law. The experimental observation of an exponential *I-V* characteristic in BSCCO [cf. Eq. (1)] might be caused by an increasing deviation from the equilibrium distribution function, $f(E)$, at high bias currents. The single junction normal state resistance $R_n = 1.85\ \Omega$ corresponds to a *c*-axis resistivity $\rho = 31.5\ \Omega$ cm (taking the thickness of a single junction as 15 Å). This value is comparable to the value that would be deduced from an extrapolation of the *c*-axis resistivity above T_c. A similar comparison between theoretical tunneling characteristic and experimental data for TBCCO is shown in Fig. 5(c) with $\Delta_0 = 25$ meV and $R_n = 66.7\ \Omega$.

The authors of Refs. 15 and 16 have also compared the intrinsic *I-V* characteristic to a tunneling characteristic with a $d_{x^2-y^2}$ density of states. However, in these works the measured *I-V* curves used for the fits represented more than one junction in the resistive state. In Ref. 16 the *I-V* characteristic with five junctions in the resistive state is compared to the calculated curve and comes close to our result for the single junction. However, with only one junction in the resistive state, thermal heating effects are minimized so that the measured characteristic offers a higher reliability. Furthermore, in contrast to the analyses in Refs. 15 and 16, we did not introduce an additional fitting parameter for a parallel leakage current.

The magnitude of the supercurrent is an important quantity of the insulating barrier and should be related to its normal state resistance R_n. The low temperature I_cR_n product for a junction between two identical *s*-wave superconductors was calculated by Ambegaokar and Baratoff to be $I_cR_n = \pi\Delta/2e$.[24] The I_cR_n product for a *c*-axis intrinsic Josephson junction where the superconductors are modeled as identical *d*-wave superconductors is theoretically calculated to be approximately Δ/e.[25] Whereas the critical current can be determined directly from experimental data, the normal state resistance is hard to access for a stack of junctions. The reason is that usually many junctions switch to the resistive state before the gap edge of the first junction is reached. The authors of Ref. 16 were able to observe a transition to a linear dependence at $V = 285$ mV with a stack of five intrinsic junctions, hence determining the gap voltage for each junction to be $2\Delta_0/e = 57$ mV. This value is similar to that chosen as the input parameter for calculating the quasiparticle tunneling current earlier. Regarding the gap value, it should be noted that in Ref. 11 a significantly smaller value of $2\Delta/e = 20$–26 mV was proposed.

From our data on BSCCO mesas and TBCCO step stacks we can find a value for R_n and hence I_cR_n by comparing the measured part of the *I-V* characteristic with one junction in the resistive state with the theoretical curve, as shown in Fig. 5. For BSCCO sample Z4gt5 we get $R_n = 1.85\ \Omega$ [see Fig. 5(b)] and the I_cR_n product can be estimated to be about 3.1 mV $\approx \Delta/8e$, i.e., significantly smaller than the theoretically predicted value Δ/e. In the same manner we determined the I_cR_n products for the other samples investigated. The results for the BSCCO samples vary between 1.5 mV and 3.1 mV (cf. Table I) and are similar for TBCCO. The value of the normal state resistance R_n determined from Eq. (2) clearly depends on the choice of Δ_0, the fitted value R_n decreasing for increasing Δ_0. The majority of published values for Δ_0 lie between 25 meV and 30 meV. Taking the higher boundary value $\Delta_0 = 30$ meV causes the fitted values for R_n and thus I_cR_n to decrease to about 70% of the value determined with $\Delta_0 = 25$ meV. Hence, the discrepancy between theory[25] and I_cR_n as determined from the measured *I-V* characteristic becomes even larger.

The small values of I_cR_n are supported by an experiment in a different configuration.[39] In these experiments, several Pb electrodes were evaporated onto one *a-b* face of a BSCCO single crystal in order to investigate *c*-axis super-

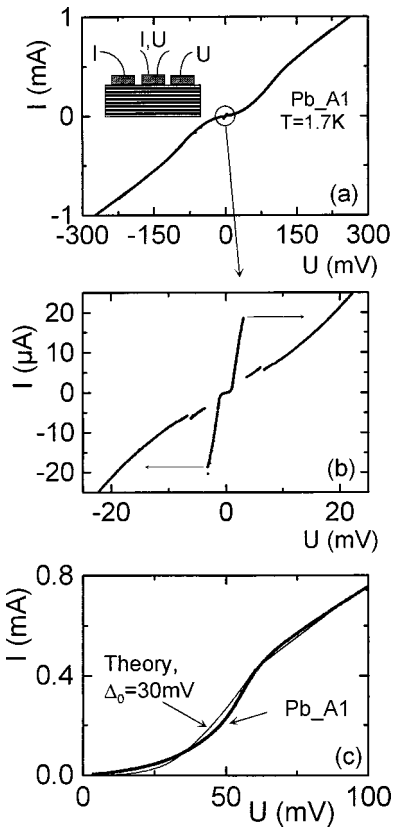

FIG. 6. *I-V* characteristic of a single intrinsic junction in a BSCCO single crystal in series with a Pb/BSCCO junction on (a) a 300 mV scale (inset shows sample geometry) and (b) on a 20 mV scale. Note the appearance of the Pb gap in (b). (c) Same *I-V* characteristic after numerical subtraction of the voltage across the Pb/BSCCO junction. Solid line is the calculated quasiparticle tunneling characteristic between two *d*-wave superconductors with $\Delta_0 = 30$ meV.

currents between Pb and BSCCO (Fig. 6, inset). If the surface of the BSCCO crystal were perfectly flat, the only voltage drop would occur at the Pb/BSCCO interface. However, due to growth steps underneath the Pb/BSCCO junctions, the real geometry consisted of ''mesas'' containing the Pb/BSCCO junction as well as a few intrinsic junctions. In one experiment, the *I-V* characteristic of a single intrinsic junction in series with the Pb/BSCCO could be measured up to 300 mV [Fig. 6(a)]. The critical current of the intrinsic junction was 20 μA [Fig. 6(b)]. On a mA scale the gap structure of the intrinsic junction can clearly be seen [Fig. 6(a)]. The figure also clearly shows that the critical current is highly suppressed relative to the gap edge. After correcting for the voltage drop across the Pb/BSCCO junction, we find reasonable agreement with theory [Fig. 6(c)]. For this junction we find $R_n = 140\ \Omega$ and thus $I_c R_n \approx 2.8$ mV, in good agreement with our previous estimate.

B. Temperature dependence of the *I-V* characteristic

The temperature dependence of the *I-V* characteristic of a BSCCO sample is shown in Fig. 7(a). The temperatures range from $T = 4.2$ K to 65 K. At higher temperatures the *I-V* characteristic is nonhysteretic and, due to the large contribution of rectified ac Josephson currents, pure quasiparticle

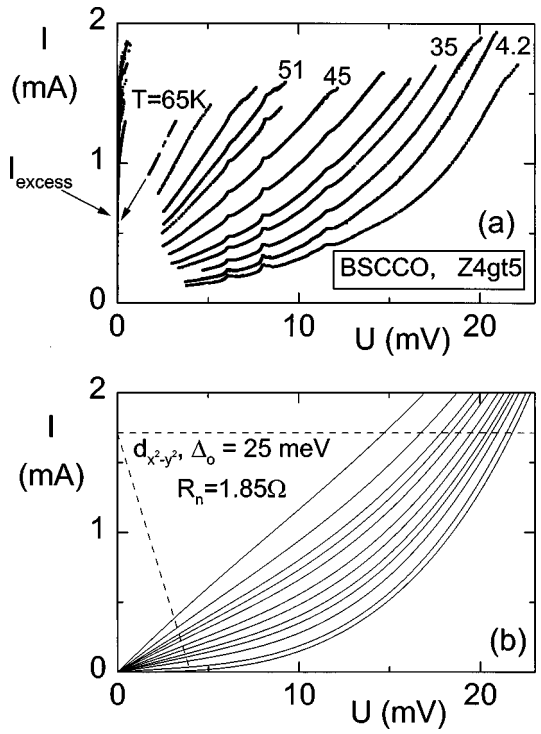

FIG. 7. (a) *I-V* characteristics of a mesa on a BSCCO single crystal with only one junction in the resistive state at temperatures $T = 4.2$, 20, 30, 35, 38, 41, 45, 49, 51, 54, 58, and 65 K. For the highest temperature the pronounced excess current is indicated. (b) Calculated *I-V* characteristics for the same set of temperatures between $T = 4.2$ K and $T = 65$ K. The temperature dependence of the gap value was neglected. The dashed lines indicate the critical current and the experimentally observed temperature dependence of the switching voltage to the superconducting state.

tunneling cannot be investigated. A similar set of intrinsic *I-V* characteristics of a TBCCO step stack sample is shown in Fig. 8.

At low temperatures ($T < 30$ K) the quasiparticle branch changes only slowly with temperature [cf. Fig. 7(a)]. At higher temperatures it changes more rapidly. The critical current decreases only slightly, but the hysteresis decreases rapidly. In BSCCO, at $T = 65$ K, the quasiparticle branch is almost linear but does not extrapolate to zero current at zero voltage. The origin of this extrapolated excess current at zero

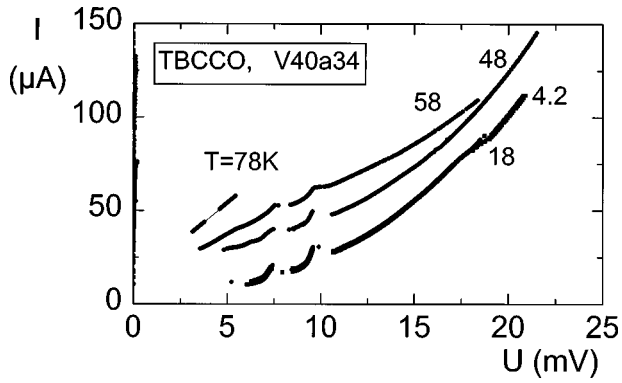

FIG. 8. *I-V* characteristics of a TBCCO step stack sample with only one junction in the resistive state at temperatures $T = 4.2$, 18, 48, 58, and 78 K.

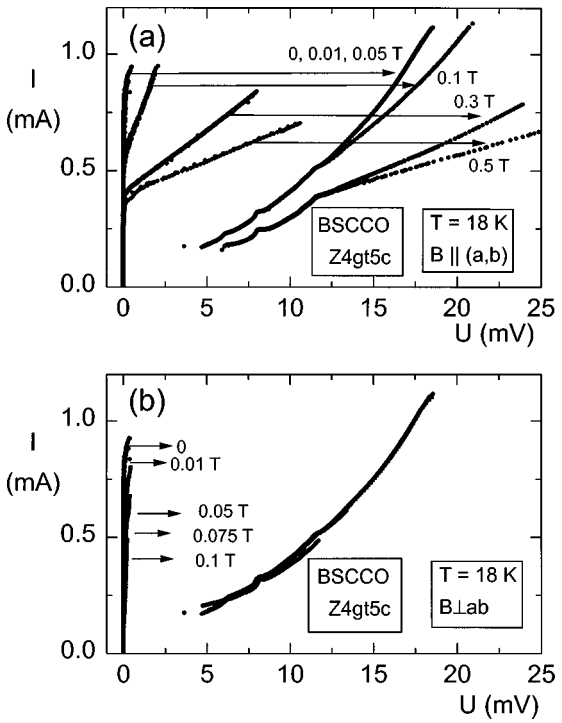

FIG. 9. *I-V* characteristic (first resistive branch) of a BSCCO mesa in different magnetic fields (a) parallel and (b) perpendicular to the layers. The arrows indicate the critical current in different external fields.

voltage is unclear. According to a model by Blonder, Tinkham, and Klapwijk[59] it could be argued to be due to Andreev reflections inside the barrier between the two superconductors.

The experimentally observed temperature dependence can also be compared to the calculated tunneling characteristics at higher temperatures. Figure 7(b) shows the calculated *I-V* characteristics of Eq. (2) at different temperatures up to $T=65$ K. As experimental investigations of the temperature dependence of the energy gap have shown that the gap value is nearly constant up to about $0.8T_c$,[60,61] we have neglected the temperature dependence of the gap in our calculations as well as the temperature dependence of the normal state resistance R_n. The dashed lines indicate the critical current and the experimentally observed temperature dependence of the switching voltage to the superconducting state. The set of calculated *I-V* characteristics reproduces qualitatively the experimentally observed temperature dependence including the transition to a linear branch at higher temperatures.

C. Magnetic field dependence of the *I-V* characteristic

As the quasiparticle branch is determind by the tunneling current, it should not be affected by external magnetic fields. To orient the sample accurately we made use of the lock-in transition, which is observed only in a very restricted angle range around the parallel orientation.[7] In Figs. 9(a) and 9(b), the *I-V* characteristics for field directions parallel and perpendicular to the layers are plotted for different field strengths. For the parallel orientation, the superconducting branch shows a transition to finite voltages with a linear dependence before exceeding the critical current and switching to the quasiparticle branch. This Josephson flux flow effect was investigated in detail by Hechtfischer *et al.*[7] Due to Josephson vortex motion in junctions that have not switched to the quasiparticle branch, there is an additional voltage drop across the stack. This voltage adds to the pure tunneling branches. For magnetic fields below 0.05 T the flux flow did not occur. Thus, the three quasiparticle branches measured for $B=0$, 0.01, and 0.05 T coincide completely. For $B=0.1$ T, flux flow occurs for currents larger than 0.6 mA leading to a deviation of the quasiparticle branch at larger current values. However, the part of the curve measured at lower currents has not changed. The two curves measured at 0.3 and 0.5 T form a separate family of branches, but in principle they exhibit the same shape. We attribute the appearance of two bundles of quasiparticle branches to the observation of two different junctions in the stack, i.e., at higher fields another junction with a slightly different critical current (due to inhomogeneities or trapped flux) is observed. The curvature of the *I-V* characteristic is not affected by the magnetic field, as expected for quasiparticle tunneling.

In the perpendicular field orientation the critical current decreases much more rapidly with increasing field. The curvature of the quasiparticle branch, however, is not affected.

IV. SUBGAP STRUCTURES IN THE *I-V* CHARACTERISTIC

Well below the gap value $2\Delta_0/e\approx 50$ mV, the quasiparticle branches of the intrinsic Josephson junctions exhibit pronounced subgap structures. Figure 10 shows the *I-V* characteristic of an intrinsic junction stack in BSCCO, the magnification of the low current region revealing the extremely regular subgap structures. First reports on these structures in intrinsic junctions in BSCCO as well as TBCCO were published in Refs. 3–5 and for the BSCCO compound independently by Yurgens *et al.*[10] The voltage positions V_1^a and V_1^b of the two most pronounced structures are 6.15 mV and 8.05 mV in BSCCO (Refs. 4 and 10) and 7.5 mV and 9.6 mV in TBCCO.[4] These main structures can be seen directly in the *I-V* characteristic (cf. Figs. 3, 4, 7, and 10) and usually exhibit a hysteresis. The apparent splitting of the structures in branches of higher order is a direct consequence of this hysteresis plus the assumption of independent stacked junctions, as will be shown in Sec. IV A. Additionally, less pronounced structures were observed in measurements of the differential resistance dV/dI. This is discussed in Sec. IV B. For data evaluation we chose to define the minima in the differential resistance dV/dI as the voltage positions of the less pronounced structures. For the more pronounced hysteretic structures the switching voltage provides a sharper criterion. The differences between the two criteria were less than 0.1 mV ($\approx 1\%$).

In order to assign an intensity to the structures, we defined the intensity by the maximum excess current above the linear extrapolated unperturbed characteristic (background current) (cf. Fig. 11). The intensities even of the most pronounced structures are not higher than a few percent of the critical current. For the ratio of the intensities of the two main structures in BSCCO at voltages $V_1^a=6.15$ mV and $V_1^b=8.05$ mV, we find $\Delta I_1^a:\Delta_1^b\approx 3:5$.

The voltage positions of the subgap structures in the *I-V*

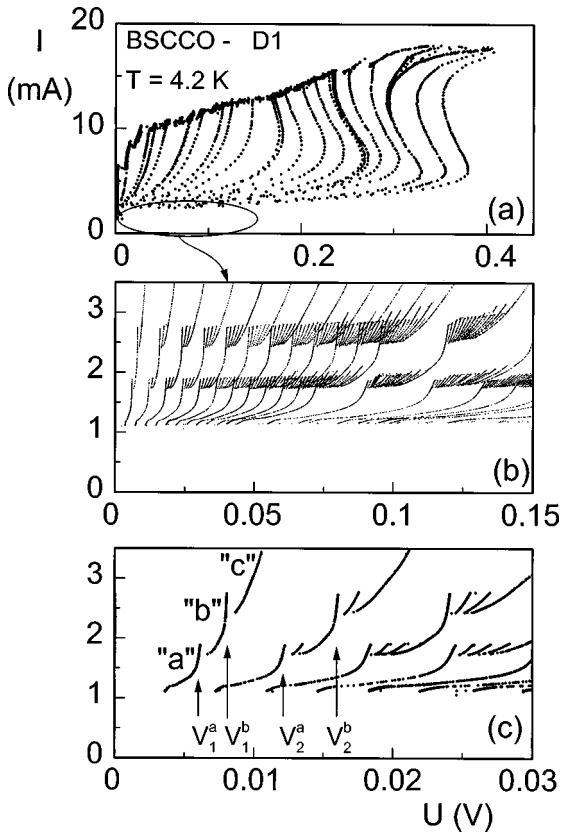

FIG. 10. (a) I-V characteristic of a BSCCO mesa at $T=4.2$ K. Not all branches are traced out. With increasing number of resistive junctions, heating effects cause a backbending of the I-V curve. (b) Enlargement of the region indicated in (a) showing the extremely regular structures in all branches. (c) The same data on an expanded scale with the sub-branches a, b, and c and the structure voltages V_1^a, V_1^b, V_2^a, and V_2^b marked.

characteristics of all samples investigated are listed in Table II. The scatter between different samples is less than 2%. Moreover, not only are the voltages absolutely reproducible, but so too is the curvature of the structures. This is demonstrated in Fig. 12, where the first resistive branch of the I-V characteristics of two step stack samples on different TBCCO films is plotted. The current axes are scaled appropriately to allow a comparison between the different sized samples.

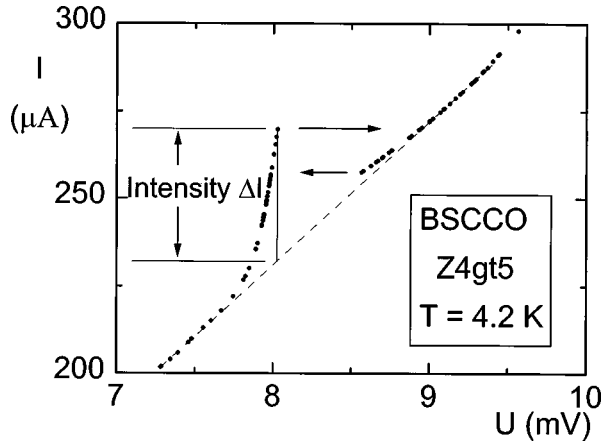

FIG. 11. Part of a BSCCO I-V characteristic indicating the method used to assign an intensity ΔI to the subgap structures.

We present the results of our investigation of these structures as a function of sample geometry and number of resistive junctions (Secs. IV A and IV B), temperature (Sec. IV C), magnetic field both parallel and perpendicular to the layers (Sec. IV D), doping (Sec. IV E), and microwave properties (Secs. IV F and IV G). The subsequent discussion (Sec. IV H) summarizes conventional explanations for the structures and presents a theoretical model involving the interaction between oscillating Josephson currents and infrared active optical c-axis phonons.

A. Multiplicity of the subgap structures

There are two hysteretic regions on each branch. On the first branch we observe two voltage jumps with increasing bias current, at voltages denoted V_1^a and V_1^b in Fig. 10(c). In BSCCO, $V_1^a = 6.15$ mV and $V_1^b = 8.05$ mV; in TBCCO, $V_1^a = 7.5$ mV and $V_1^b = 9.6$ mV. On the nth branch, corresponding to n junctions being resistive, there are n hystereses in each region. This can easily be explained by assuming that the I-V characteristic of each individual junction consists of three sub-branches denoted ''a,'' ''b,'' and ''c'' in Fig. 10(c). At voltages below $V_2^a \approx 2V_1^a$ on the second branch both resistive junctions are on their sub-branch ''a.'' After the first voltage jump one junction has switched to branch ''b,'' and after the second jump both junctions are on their sub-branch ''b.'' At $V_2^b \approx 2V_1^b$ first one and finally both junctions switch to ''c.'' The possible combinations of voltages with two resistive junctions having identical I-V characteristics are illustrated in Fig. 13. The combinations of sub-branches ''a,'' ''b,'' and ''c'' appear as five distinct sub-branches ''aa,'' ''ab,'' ''bb,'' ''bc,'' and ''cc'' in the total or combined I-V characteristic. To verify this directly from the experimental data we compare the voltages of the experimentally measured first branch with the voltage difference between the first and second branches (see Fig. 14). If the model in Fig. 13 is correct, these two branches should be equivalent. Referring to Fig. 14, it can be seen that the differences ''aa''-''a'' and ''ab''-''b'' coincide with ''a,'' ''bb''-''b'' and ''bc''-''c'' with ''b,'' and ''cc''-''c'' with ''c.'' Thus the multiplicity of the subgap structures in the $n=2$ branch is a simple consequence of possible voltage combinations.

This is also the case for higher order branches. As an example, Fig. 15 shows the $n=22$ branch where all 22 subbranches due to the 22 possible voltage combinations can be seen. To allow a direct comparison between the $n=1$ and the $n=22$ branches, the measured voltages of the $n=22$ branch have been divided by 22 in the lower half of the figure. With this scaling, it can be seen that the series of sub-branches start at the same position for both branches. Similarly, we observed in branch $n=50$ a total number of 50 sub-branches starting from a voltage equal to $50V_1^a$ (Fig. 16). We conclude that *all* junctions in the crystal show subgap structures and that their position is independent of the number of junctions in the resistive state.

TABLE II. Properties of investigated samples including lateral sizes, critical temperatures, and voltage positions of the two main subgap structures V_1^a and V_1^b of the different $Bi_2Sr_2CaCu_2O_{8+\delta}$ mesas and $Tl_2Ba_2Ca_2Cu_3O_{10+\delta}$ step stacks, respectively. The samples Z4gt5, -b, -c are three different mesas on top of the same crystal annealed for 4 h at 550 °C in air. Samples denoted by an asterisk were annealed for 10 h at 350 °C in air.

$Bi_2Sr_2CaCu_2O_{8+\delta}$ mesas				
Sample	Size (μm^2)	T_c (K)	V_1^a (mV)	V_1^b (mV)
D6a	40 × 40	91	6.02 ± 0.05	7.90 ± 0.05
D9b	20 × 20	87	6.05 ± 0.05	7.97 ± 0.05
D6	20 × 20	88	5.95 ± 0.5	7.97 ± 0.5
D6*	20 × 20	80	6.15 ± 0.05	8.05 ± 0.05
D1*	40 × 40	84	6.16 ± 0.05	8.06 ± 0.05
D7*	40 × 40	87	6.09 ± 0.05	8.05 ± 0.05
Z4gt5	16 × 16	86	6.11 ± 0.05	8.06 ± 0.05
Z4gt5b	16 × 16	86	6.11 ± 0.05	8.06 ± 0.05
Z4gt5c	16 × 16	86	6.10 ± 0.05	8.04 ± 0.05
$Tl_2Ba_2Ca_2Cu_3O_{10+\delta}$ step stacks				
Sample	junction width (μm)	T_c (K)	V_1^a (mV)	V_1^b (mV)
V40a1	10	109	7.43 ± 0.2	9.65 ± 0.2
V40a34	9	109	7.43 ± 0.05	9.60 ± 0.05
V75a12	12	108	7.65 ± 0.05	9.65 ± 0.05
V75b24	24	115	7.57 ± 0.1	9.60 ± 0.1
V86c7	15	115	7.44 ± 0.05	9.64 ± 0.05
V91c1	5	114	7.54 ± 0.05	9.71 ± 0.05
V91c8	5	114	7.36 ± 0.1	9.57 ± 0.1

B. Less pronounced subgap structures

The less pronounced structures, although apparent in the *I-V* characteristic, are revealed more clearly in measurements of the differential resistance. Figure 17 shows both the *I-V* characteristic and the differential resistance of the first branch in a BSCCO mesa. The additional voltage due to the contact resistance in measurements made in a two-terminal configuration has been subtracted on the voltage axis. The contact resistance also adds as an offset to the measured differential resistance dV/dI. This offset for the dV/dI data has not been subtracted. Therefore, the absolute values should be interpreted carefully.

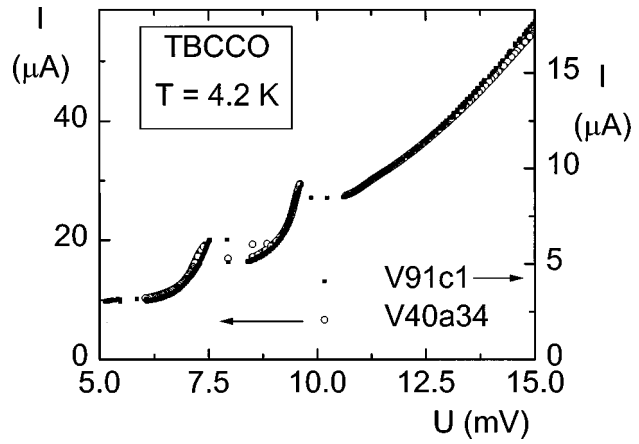

FIG. 12. Comparison of the first resistive branch of the *I-V* characteristics of two different TBCCO step stack samples in the voltage range of pronounced subgap structures showing the extremely good reproducibility of the resonant upturns.

To establish that the structures in dV/dI are not an artefact of the contact resistance, it is necessary to demonstrate that the structures also appear in branches of higher order at voltages proportional to the branch number. The *I-V* characteristic and differential resistance of the second and fifth branch of a BSCCO mesa are plotted in Fig. 18. To allow a comparison, the voltage axes are scaled in the ratio 2:5. Note that the less pronounced structures appear to be nonhysteretic and do not exhibit the splitting observed in the main structures of the higher order branches. All structures in the second branch can also be seen in the fifth branch at voltages that are a factor of 5/2 times greater. This clearly shows that the structures in dV/dI are not an artefact but again an in-

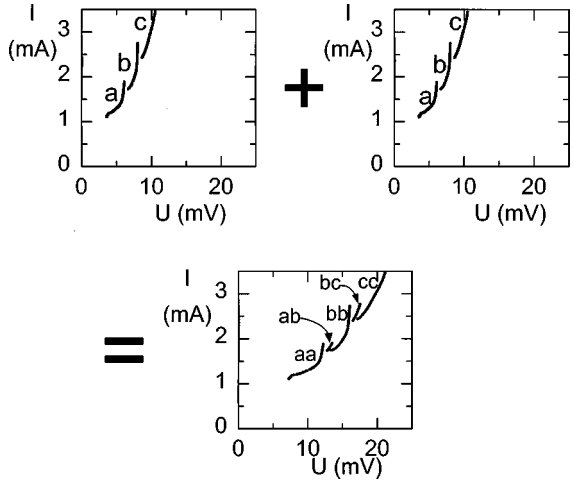

FIG. 13. The multiplicity of the subgap structures as a consequence of possible voltage combinations (see text for explanation).

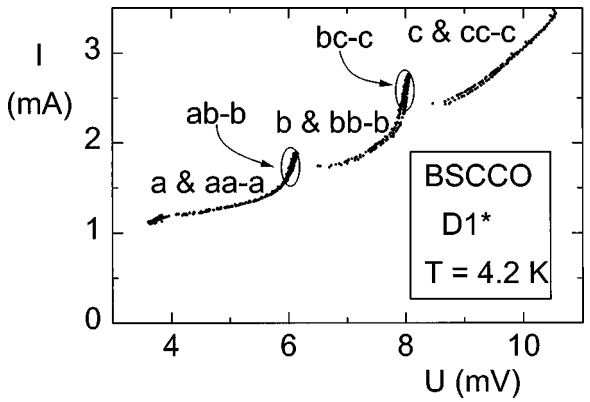

FIG. 14. Comparison of the voltages of the experimentally measured first branch to the voltage difference between the first and second branches for BSCCO sample D1* The sub-branch ''*aa*''-''*a*'' coincides with ''*a*,'' ''*ab*''-''*b*'' with ''*a*,'' ''*bb*''-''*b*'' with ''*b*,'' ''*bc*''-''*c*'' with ''*b*,'' and ''*cc*''-''*c*'' with ''*c*.''

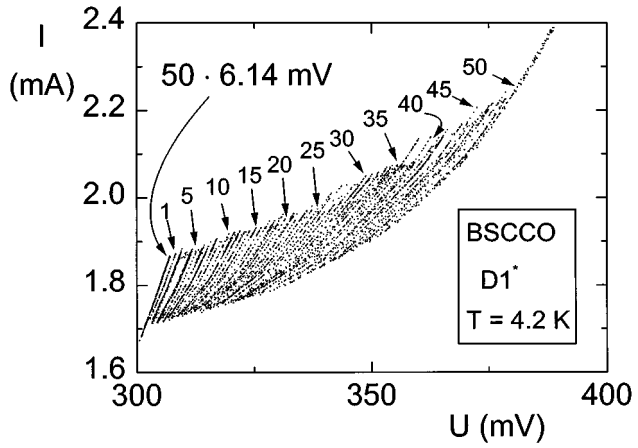

FIG. 16. Branch No. 50 of a BSCCO mesa exhibiting a series of 50 sub-branches starting from a voltage equal to 50 V_1^a.

trinsic property of every junction. The minima in the differential resistance for these less pronounced structures together with those of the main structures and the frequencies $f=(2e/h)V$ of the corresponding ac Josephson currents are listed in Table III.

There are several effects known to cause a series of structures in the *I-V* characteristics of Josephson junctions. Multiple Andreev reflections,[62] incoherent many particle tunneling,[63] and Josephson self-detection[64] produce structures at voltages that are connected to the gap voltage $2\Delta/e$ via a subharmonic $(1/n)$ series. However, the voltage positions of the structures observed in the *I-V* characteristic of intrinsic Josephson junctions do not form a subharmonic series. Also, their intensity would be expected to decrease rapidly with increasing order n, i.e., with decreasing voltage, which is not the case in the experiment. We therefore rule out the above mentioned processes as explanations for the observed structures in the *I-V* characteristic.

In the discussion that follows we consider only the main structures, where data evaluation can be performed with higher accuracy.

C. Temperature dependence of the subgap structures

If the voltages of the structures are related to the energy gap of the superconducting state, a similar temperature dependence can be expected for the two quantities. At least at temperatures close to T_c where the gap decreases rapidly, the voltage position of the structures should also show a clear decrease. As can be seen in Fig. 7, the voltage positions of the subgap structures remain unchanged up to about 50 K. However, with increasing temperature the characteristic voltage jump V_c decreases much more rapidly and at about $T=50$ K it crosses the voltage of the subgap structures (Fig.

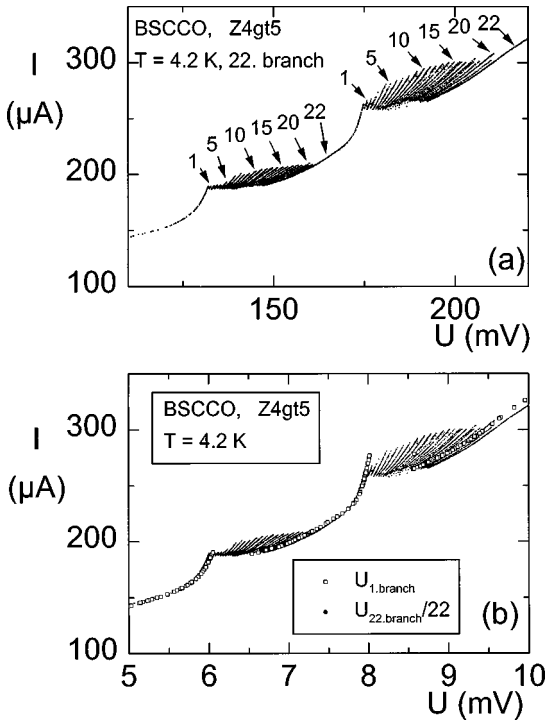

FIG. 15. (a) Selected area of the *I-V* characteristic of a BSCCO mesa showing the $n=22$ branch with the two regions of hysteretic subgap structures. (b) As in (a) but with voltage values divided by a factor of 22 to allow comparison to the $n=1$ branch.

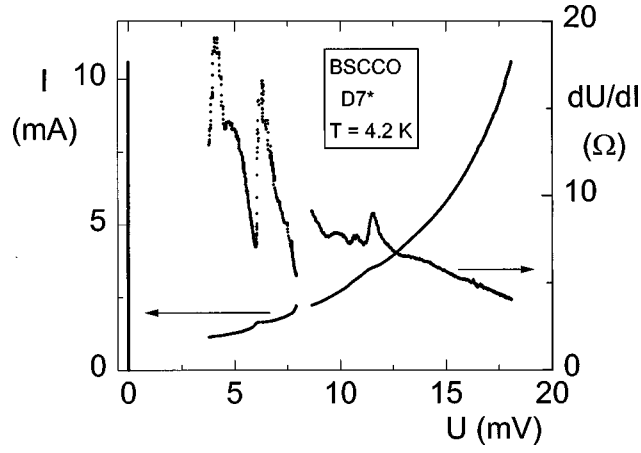

FIG. 17. *I-V* characteristic (left scale) and differential resistance (right scale) of the first branch of BSCCO mesa D7*. In addition to the main structures, several additional minima in the differential resistance can be seen.

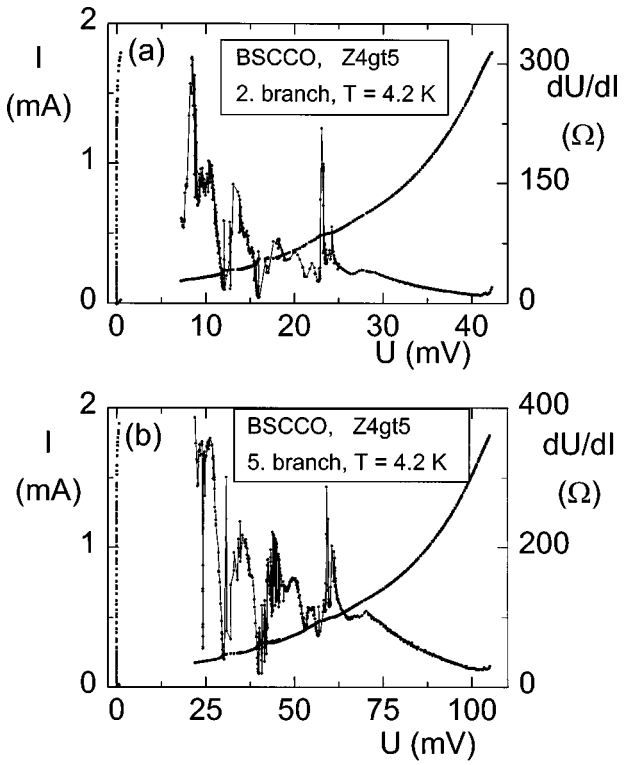

FIG. 18. *I-V* characteristic (left scale) and differential resistance (right scale) of (a) the second and (b) fifth branch of BSCCO mesa Z4gt5. The voltage axes are scaled by the ratio 2:5 in order to show that the less pronounced structures also appear in all branches.

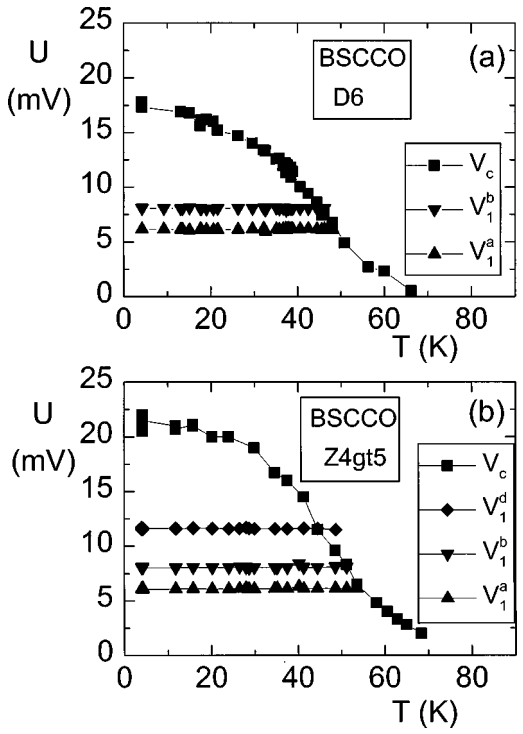

FIG. 19. Voltage jump V_c and voltage position of the main structures V_1^a and V_1^b in the *I-V* characteristic vs temperature for two different BSCCO samples. For sample Z4gt5, a third structure V_1^d at 11.6 mV was evaluated.

19). If the voltage is increased above the characteristic voltage V_c, the next junction switches into the resistive state making a further investigation of the structures impossible.

A temperature increase only results in a decreased hysteresis of the subgap structures. The intensity as defined in Fig. 11 remains essentially constant, as shown in Fig. 20. If the structures are caused by a peak in the quasiparticle current — e.g., due to subgap peaks in the density of states[4] — thermal smearing should manifest itself as a small decrease of the intensity. Because of the data scattering, a slight decrease of the intensity cannot be excluded. In the relevant temperature range up to 50 K, the critical current also changes only slightly [Figs. 20(c) and 20(d)], compatible with a possible proportionality between intensity and critical current.

If the structures are caused by scattering processes with thermally excited quasiparticles, the intensity should exhibit a strong temperature dependence. This can be clearly excluded by the experimental data. However, this does not rule out interaction mechanisms with quasiparticles such as phonons, which are externally excited by the Josephson field oscillations, as will be discussed below.

D. Magnetic field dependence of the subgap structures

If the structures are caused by geometric self-resonances of the supercurrent as, e.g., Fiske resonances[65] or zero field steps,[66] the voltage position of these structures should be inversely proportional to the junction width and, in the case of flux flow steps,[67] the voltage should depend on the mag-

TABLE III. Voltage positions of subgap structures in the *I-V* characteristic of intrinsic junctions in $Bi_2Sr_2CaCu_2O_{8+\delta}$ at $T=4.2$ K. The table shows the voltages of minima in the differential resistivity. In measurements with sample D6a, we were able to detect additional structures at 3.13 mV and at higher temperatures also at 1.68 mV and 2.57 mV. The last line displays the frequencies $f=2$ eV/h of the corresponding ac Josephson currents.

Sample	Minima in differential resistivity (mV)										
D1*	3.98	4.63	4.97	6.07	7.19	7.53	7.98	9.67	10.65	11.59	13.25
D6a	3.86	4.65		6.06	7.13	7.45	7.93	9.63	10.67	11.47	13.15
D6*				5.95			8.03	9.62	10.8	11.6	
D7*	3.87	4.55		6.06	7.19	7.55	7.99	9.56	10.71	11.58	13.09
Z4gt5	3.77	4.58	4.99	6.06	7.22	7.50	8.00	9.63	10.65	11.81	13.27
f (THz)	1.87	1.98	2.38	2.97	3.47	3.63	3.89	4.65	5.17	5.60	6.38

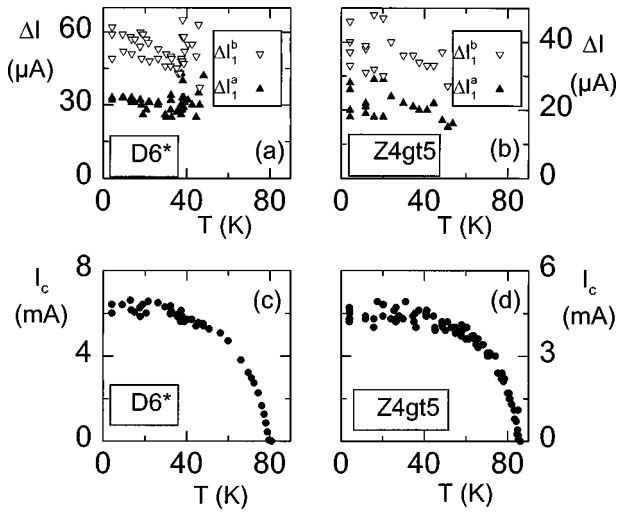

FIG. 20. Intensity ΔI vs temperature for the two main structures at V_1^q and V_1^b in BSCCO samples D6* and Z4gt5 (a),(b) and critical current of the majority of the junctions in the stack vs temperature for the same samples (c),(d).

nitude of the applied magnetic field parallel to the superconducting layers.[42] The *I-V* characteristics in different magnetic fields were shown in Fig. 9. The voltage position of the structures remains constant, as is explicitly shown in Figs. 21(a) and 21(b) for different field strengths. Hence, together with the independence on junction width (cf. Table II), we conclude that the structures are not due to geometric self-resonances of the supercurrent.

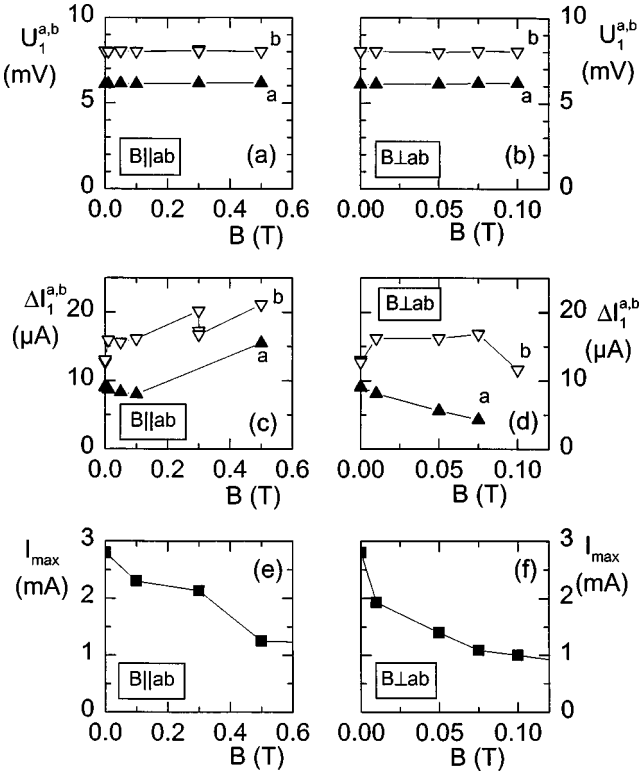

FIG. 21. (a) and (b) Voltage position of the main structures in BSCCO vs magnetic field for field orientation parallel and perpendicular to the layers. The intensities are shown in (c) and (d). (e) and (f) show the critical current for the orientation parallel and perpendicular to the field, respectively.

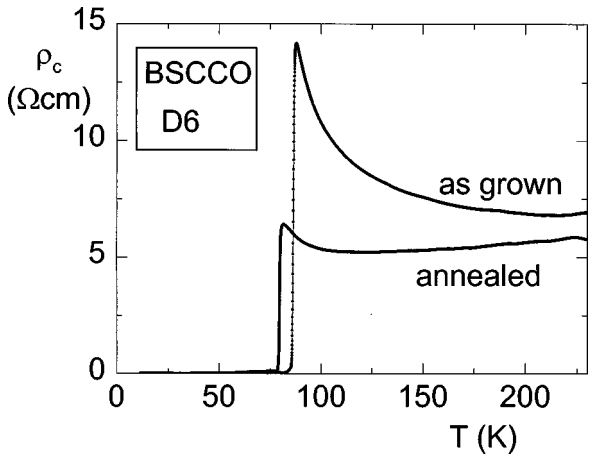

FIG. 22. Temperature dependence of the c-axis resistivity ρ_c of BSCCO sample D6* as grown and after annealing in air. Critical temperatures are 88 K (as grown) and 80 K (annealed).

The intensity of the structures with external magnetic field is plotted in Figs. 21(c) and 21(d) for the parallel and perpendicular field orientation, respectively. Again, the criterion as defined in Fig. 11 was used for the data evaluation. For both field orientations, neither a clear increase nor a decrease in the intensity can be observed. For comparison we show the maximum supercurrent for both field orientations in parts (e) and (f) of Fig. 21. In contrast to the intensity of the subgap structures, the supercurrent is significantly suppressed by the magnetic field.

E. Doping dependence of the subgap structures

In order to check the dependence of the subgap structures on the oxygen doping in the barrier, i.e., for BSCCO in the BiO layers, we have investigated the structures for BSCCO crystals under different annealing conditions. Because of the layered crystal structure of the materials investigated, one might argue that resonant tunneling processes[68] could be the origin of the structures. This effect has been observed in semiconductor superlattices,[69] for example. The voltage position of resonant tunneling structures in the *I-V* characteristic will be sensitive to the height of the potential barrier of the tunnel junction. In BSCCO our annealing process introduces excess oxygen in the BiO layers, and therefore changes to the barrier potential can be expected.

The result of the annealing process is shown in Fig. 22 by the temperature dependence of the c-axis resistivity ρ_c before and after annealing. The as-grown sample D6 with $T_c = 88$ K had a critical current density $j_c = 660$ A/cm^2 and the structures in the *I-V* characteristic were weak and nonhysteretic. After oxygen doping by annealing in air (D6*), the critical current density was raised to 1630 A/cm^2 and the critical temperature of the now overdoped sample lowered to 80 K. The subgap structures became significantly more pronounced. Importantly, however, the structures still occur at the same voltages within experimental uncertainty (cf. Table II). Thus we conclude that the observed structures in the intrinsic *I-V* characteristic are not caused by resonant tunneling processes via localized states in the barrier.

The possibility that the structures are related to superconductivity in the BiO layers, apparently observed in the highly

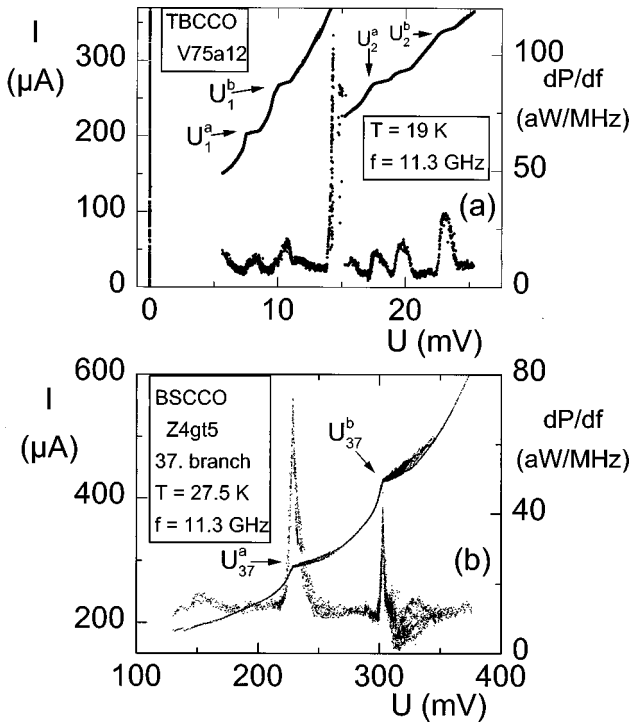

FIG. 23. (a) *I-V* characteristic (left scale) of the first and second branch of a TBCCO step stack and detected microwave power (right scale). (b) *I-V* characteristic (left scale) of the 37th branch of a BSCCO mesa and detected microwave power (right scale).

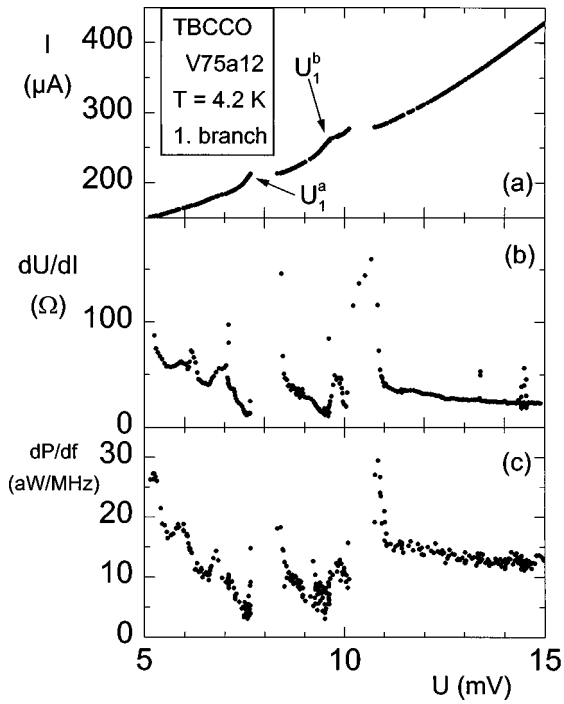

FIG. 24. Current (a), differential resistance (b), and detected microwave power (c) vs sample voltage for TBCCO sample V75a12.

overdoped state,[29] is also ruled out by the insensitivity of the voltage positions of the structures to different doping states.

F. Microwave emission at the subgap structures

In the voltage range of the subgap structures we detected microwave emission at a frequency $f=11.3$ GHz, which is about three orders of magnitude below the Josephson oscillation frequency $f=(2e/h)V\approx 3-4$ THz. An example is shown in Fig. 23(a), where the first two branches of a TBCCO step stack are plotted together with the detected microwave signal. The detected power increased with an increasing number of junctions in the resistive state. For BSCCO sample Z4gt5 we were unable to detect microwave emission in the first resistive branches, but in branches of higher order with a larger number of resistive junctions microwave emission was observed. Figure 23(b) shows branch number 37 together with two microwave emission peaks clearly related to the two groups of subgap structures. The actual location of these emission peaks is correlated to the position of the peaks in the differential resistance. This is demonstrated in Fig. 24, where the *I-V* characteristic (a), the differential resistance (b), and the detected microwave power (c) are plotted. The observed relation between microwave emission and differential resistance can be explained in terms of thermal fluctuations of the current. At points in the *I-V* characteristic with high differential resistance, the voltage fluctuations caused by thermal fluctuations of the current are amplified and lead to an enhanced microwave emission.[70]

G. Microwave absorption at the subgap structures

Under microwave irradiation, the voltage position of the subgap structures shifts, as reported recently for TBCCO by Seidel *et al.*[12] Figure 25 shows the *I-V* characteristic of a BSCCO mesa with and without microwave irradiation of frequency $f_{rf}=8.16$ GHz. It can clearly be seen that under irradiation each subgap structure splits into a pair of two structures. The first one appears at a lower voltage than the unperturbed structure, the second one at a higher voltage. The voltage positions of the splitted structures are plotted against the square root of the applied microwave power P in the inset of Fig. 25. The voltage separation between the splitted structures depends linearly on $\sqrt{P}$. With sufficient microwave power the splitting can even lead to a crossing of the voltages of the subgap structures.

The splitting and shifting of the subgap structures can easily be explained by the strong nonlinearity of the *I-V* characteristic near the subgap structure. Since the frequency of the external microwave field is much smaller than the

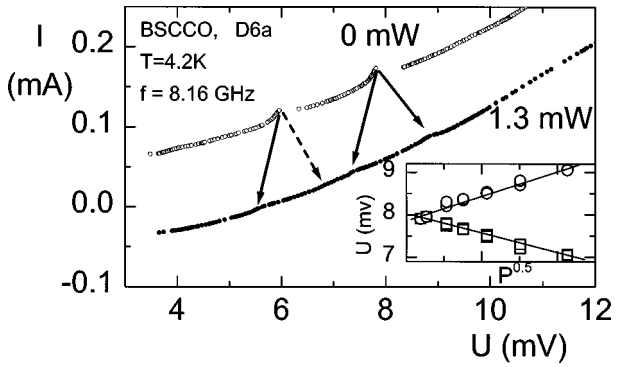

FIG. 25. *I-V* characteristic of a BSCCO mesa with and without microwave irradiation. Curves are shifted vertically for clarity. Inset shows the voltage positions of the splitted structure V_1^b vs the square root of the applied microwave power.

frequency of the Josephson oscillations, the irradiation corresponds to an ac bias current I_{rf} acting on the I-V curve around the dc bias point I_0. As a consequence, the external current

$$I = I(t) = I_0 + I_{rf}\sin(2\pi f_{rf} t) \tag{5}$$

changes almost adiabatically and the system follows the (bare) I-V curve without microwave irradiation almost immediately. Thereby the dc component

$$V_{dc} = \langle V(I(t))\rangle_t = V(I_0) + \frac{1}{2}\frac{d^2V}{dI^2}\bigg|_{I_0} \langle (I_{rf}(t))^2\rangle + \cdots \tag{6}$$

of the voltage $V(t)$ differs from the value $V(I_0)$ in the autonomous case due to the nonlinearity of the I-V curve. Thus, for a given bias current I_0 the measured dc voltage will be altered because of rectified ac voltages.

We first discuss the situation with a measured dc voltage V_{dc} smaller than the unperturbed structure voltage. As long as the voltage $V(t)$ is small enough such that the unperturbed voltage of the structure is not reached during an ac cycle, rectification should not lead to specific structures. With increasing voltage V_{dc}, however, the situation is changed as soon as $V(t)$ reaches the unperturbed structure voltage during an ac cycle. Now a structure occurs at the measured dc voltage $V_<$. With increasing ac current I_{rf} this voltage $V_<$ shifts to smaller voltages, further away from the unperturbed structure voltage.

Similar arguments can be applied for dc voltages V_{dc} larger than the unperturbed structure voltage. With $V(t)$ reaching the unperturbed structure voltage during an ac cycle, a structure occurs at the measured dc voltage $V_>$. With increasing ac current I_{rf} this voltage $V_>$ shifts to larger voltages, further away from the unperturbed structure voltage. Thus, the subgap structure splits into two structures, which separate from each other with increasing microwave power.

We will show a numerical simulation of this rectification effect in the next section, where the origin of the unperturbed structures itself is discussed in the framework of an extended RSJ model. However, it should be noted that the explanation of the experimental observations under microwave irradiation is not related to a specific model for the origin of the unperturbed structure.

H. Discussion of the subgap structures

Although all observed structures show similar parameter dependence, they are not necessarily all caused by the same effect. Nevertheless, it seems to be reasonable to look for a single explanation covering all observed structures. In the framework of the RSJ model, the total current $I = I_s + I_{qp} + I_d$ in a Josephson junction is given by the sum of the supercurrent I_s, the quasiparticle current I_{qp}, and the displacement current I_d. Thus the current density is

$$j = j_c\sin(\gamma) + \sigma E + \dot{D}, \tag{7}$$

where j_c is the critical current density, σ the electrical conductivity, and $\dot{D}$ the displacement current density. The gauge invariant phase difference γ is related to the space averaged electric field E in the barrier of thickness b by the Josephson relation

$$\dot{\gamma} = \frac{2eb}{\hbar}E. \tag{8}$$

Structures in the I-V characteristic might arise due to any of the three contributing channels in Eq. (7). First, geometric self-resonances of the supercurrent were excluded in Sec. IV D because the experimental results are independent of the junction width and external magnetic fields. Second, effects in the quasiparticle current causing structures in the I-V characteristic such as (i) multiple Andreev reflection, (ii) incoherent many particle tunneling, (iii) resonant tunneling via localized states in the barrier, or (iv) absorption processes of thermally excited quasiparticles such as phonons were excluded by different arguments discussed above. (v) In Ref. 4, an alternative model related to the layered structure was discussed. For superconductors with a periodically modulated superconducting order parameter, the quasiparticle density of states is predicted to be quite different from that of a homogeneous BCS superconductor.[71,72] Special features are a subgap peak and a modulation of the density of states at energies above the gap. Such a modulation was experimentally observed in the differential conductivity of BSCCO point contact junctions[35,36] and interpreted in a similar model as compound geometrical resonances. A subgap peak in the density of states can result in a peak in the tunneling current given by Eq. (2) and could thus in principle explain the occurrence of structures in the I-V characteristic.[4] The energy position of the subgap peaks in the density of states is predicted to be constant over a wide temperature range.[72] However, one would expect at least a small temperature dependence, i.e., a small voltage shift of the structures. Therefore, the absolute independence of the voltage position of the subgap structures observed in our I-V characteristic is hard to explain in this model. Also, a quantitative calculation including the material parameters of the high-T_c superconductors has to show whether the energy positions of this subgap peaks in the density of states are compatible with the voltage position of the observed structures in the I-V characteristic.

Our conclusion is that out of five quasiparticle effects causing structures in the I-V characteristic the models (i)–(iv) can be excluded and the model (v) seems to be questionable.

Third, resonances in the displacement current I_d remain to be considered. Recently, a natural explanation for the subgap structures in the intrinsic I-V characteristic was proposed by Helm *et al.*[73] by taking into account the coupling between infrared active c-axis phonons and Josephson oscillations. Note that in the relevant frequency range of several THz (cf. Table III), infrared active c-axis phonons were observed experimentally and calculated theoretically for both BSCCO (Ref. 74) and TBCCO.[75] The (average) electric field in the junction polarizes the ions of charge q in the barrier. This is illustrated on the right side of Fig. 26, where the layers in the $Bi_2Sr_2CaCu_2O_8$ crystal structure are denoted as superconductors and insulators, respectively. Due to the ac Josephson current, the average electric field has an oscillating component forcing the ions to oscillate. A displacement z of the

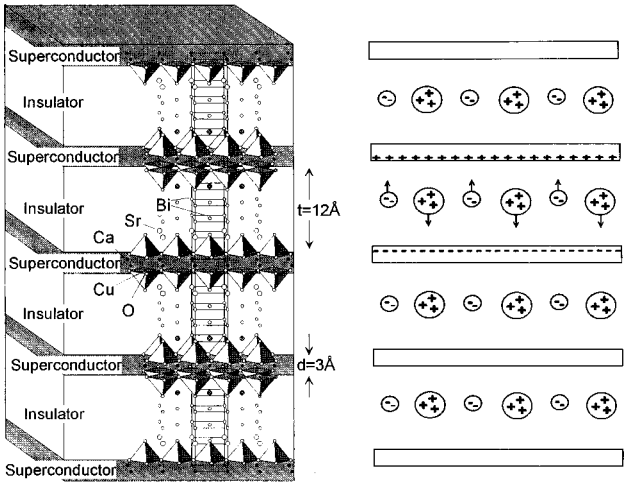

FIG. 26. Left side: model of intrinsic Josephson junctions in layered superconductors. Right side: sketch of the ionic displacement in the presence of an electric field in the Josephson junction.

ions in the barrier induces a polarization P and influences the equation of motion for the Josephson current via the last term in Eq. (7).

We describe the displacement z of the ions with mass M by a simple oscillator

$$\frac{q}{M}E_{\mathrm{loc}}=\omega_{\mathrm{LO}}^2 z+r\dot{z}+\ddot{z}, \tag{9}$$

with the oscillator eigenfrequency ω_{LO} and damping factor r modeling the dispersion in the z direction.

Note that the driving force for the oscillator is given by the local electric field E_{loc} at the position of the ion resulting from the charge fluctuations between the CuO_2 layers due to the Josephson coupling. All other Coulomb forces are already taken into account in the eigenfrequency ω_{LO} of the lattice dynamics. Because we are considering a system that is homogeneous along the x and y direction (parallel to the CuO_2 layers), the lattice vibrations only have a dispersion along the z axis and therefore only longitudinal optical phonons with eigenvectors in the c direction are excited.

The displacement D contains the ionic polarization P in the barrier:

$$D=\epsilon_0 E+P=\epsilon_0\epsilon E. \tag{10}$$

With the ionic density n we have $P=nqz$ and

$$\frac{nq^2}{M}E_{\mathrm{loc}}=\omega_{\mathrm{LO}}^2 P+r\dot{P}+\ddot{P}. \tag{11}$$

By considering the CuO_2 layers as two-dimensional superconductors, the local electric field E_{loc} and the space averaged electric field $E=1/b\int E(z)dz$ are related by

$$E_{\mathrm{loc}}=E+\frac{1}{\epsilon_0}P. \tag{12}$$

With this equation we can write Eq. (11) as

$$\frac{nq^2}{M}E=\left(\omega_{\mathrm{LO}}^2-\frac{nq^2}{M\epsilon_0}\right)P+r\dot{P}+\ddot{P}$$

or

$$\frac{nq^2}{M}\frac{\hbar}{2eb}\dot{\gamma}=\omega_0^2 P+r\dot{P}+\ddot{P}. \tag{13}$$

In this model the contribution of the oscillator to the dielectric function is given by

$$\epsilon(\omega)=\epsilon_\infty+\frac{S\omega_0^2}{\omega_0^2-\omega^2-ir\omega}, \tag{14}$$

where $S=nq^2/(\epsilon_0 M\omega_0^2)$ is the oscillator strength of the phonon and ϵ_∞ includes all other contributions to the polarizability of the barrier. In this form it is straightforward to generalize the calculation to several phonon branches and more general lattice dynamical models.

The system is characterized by the resonance frequency ω_0, the bare Josephson plasma frequency $\omega_J^2=2ebj_c/(\hbar\epsilon_0)$, and a characteristic frequency $\omega_c=(2e/\hbar)V_c$, V_c being the voltage at the critical current density j_c. In our case $\omega_J<\omega_0<\omega_c$ and the McCumber parameter $\beta_c=\omega_c^2/(\omega_J^2/\epsilon_\infty)$ is large. Note that now $\omega_0\neq\omega_{\mathrm{LO}}$ but the zeros of the phonon dielectric function are still exactly at the LO eigenfrequencies ω_{LO}.

With the Josephson relation (8) in Eq. (7) we obtain together with Eq. (13) a coupled set of differential equations for the phase difference γ and the polarization amplitude P, which can be solved numerically. By calculating the time average of $V(t)=E(t)/b$ for different dc bias current densities j, the I-V characteristic including the effect of the oscillating ions is obtained.

From the numerical results it turns out that both the phase $\gamma(t)$ and the polarization $P(t)$ oscillate primarily with one frequency, which is in agreement with general expectations for the RSJ model with large β_c.[51] Therefore, neglecting higher harmonics we use the ansatz

$$\gamma=\gamma_0+vt+\gamma_1\sin\,\omega t, \tag{15}$$

$$P=P_0+P_1\cos(\omega t+\varphi). \tag{16}$$

Here v is the time averaged phase velocity corresponding to the dc voltage $v=\langle V\rangle 2e/\hbar$ in the resistive state.

The different Fourier components of the equations of motion are obtained by the Bessel function expansion

$$\sin\,\gamma(t)=\sum_{n=-\infty}^{\infty}J_n(\gamma_1)\sin(\gamma_0+vt+n\omega t). \tag{17}$$

The Josephson current contributes to the dc current only, if $v+n\omega=0$ ($n=-1$ corresponding to the leading harmonic). Using this ansatz in the differential equations (7) and (13) we obtain a set of equations for the amplitudes of the different Fourier components. As Eq. (13) is linear in the polarization P, we can eliminate the polarization P and get an equation of motion for the phase oscillation alone:

$$0=[J_0(\gamma_1)-J_2(\gamma_1)]\cos\gamma_0-\left(\frac{\omega}{\omega_J}\right)^2\epsilon_1\gamma_1, \tag{18}$$

$$0 = J_1(\gamma_1)\sin\,\gamma_0 + \frac{1}{2}\left(\frac{\omega}{\omega_J}\right)^2\left(\epsilon_2 + \frac{\sigma}{\epsilon_0\omega}\right)\gamma_1^2, \tag{19}$$

$$j = j_{\rm qp}(V) - j_c J_1(\gamma_1)\sin\,\gamma_0, \tag{20}$$

where ϵ_1, ϵ_2 are the real and imaginary part of the phonon dielectric function (14), respectively.

As the numerical solution of Eqs. (7) and (13) shows that $\gamma_1 < 0.1$, Eqs. (18)–(20) can be linearized in γ_1 and an analytical formula for the I-V characteristic can be obtained:

$$j(V) = j_{\rm qp}(V) + \Delta j(V) = j_{\rm qp}(V) + \frac{1}{2} j_c \left(\frac{\omega_J}{\omega}\right)^2 \frac{\epsilon_2 + \dfrac{\sigma}{\omega\epsilon_0}}{\epsilon_1^2 + \left(\epsilon_2 + \dfrac{\sigma}{\omega\epsilon_0}\right)^2} \tag{21}$$

$$= j_{\rm qp}(V) - \frac{1}{2} j_c \left(\frac{\omega_J}{\omega}\right)^2 {\rm Im}\left(\frac{1}{\tilde{\epsilon}(\omega)}\right) \tag{22}$$

with $\tilde{\epsilon} = \epsilon_1 + i(\epsilon_2 + \sigma/\omega\epsilon_0)$ and $\omega = (2e/\hbar)V$.

Taking into account the second harmonic in the ansatz (15) and (16), we obtain for the I-V curve instead of Eq. (22)

$$j(V) = j_{\rm qp}(V) - \frac{1}{2} j_c \left(\frac{\omega_J}{\omega}\right)^2 {\rm Im}\left\{ \frac{1}{\left(\tilde{\epsilon}(\omega) - \dfrac{1}{16}\dfrac{\omega_J^4}{\omega^4 \tilde{\epsilon}(2\omega)}\right)} \right\}. \tag{23}$$

Higher harmonics turn out to be corrections in higher orders of $(\omega_J/\omega)^4$ and are therefore negligible for large values of the McCumber parameter $\beta_c \gg 1$. For much smaller values of the McCumber parameter ($\beta_c \approx 1$), small structures in the I-V characteristic at exactly half of the LO eigenfrequency appear due to the second harmonic.

A comparison between the measured data and the numerically and analytically calculated I-V characteristic is shown in Fig. 27. In order to reproduce the experimental data in full detail, for the quasiparticle current in BSCCO an exponential behavior

$$j_{\rm qp}(\dot{\gamma}) = j_c \exp\left(\frac{\dot{\gamma} - 1}{v_b}\right) \tag{24}$$

and in TBCCO

$$j_{\rm qp}(\dot{\gamma}) = j_c \frac{2\dot{\gamma}}{1 + \exp\left(\dfrac{1 - \dot{\gamma}}{v_b}\right)} \tag{25}$$

is assumed. For the used parameters no influence of the higher harmonics on the I-V curve is observed, as expected from the discussion above. The prediction for the eigenfrequencies $\nu_{\rm LO} = \omega_{\rm LO}(\vec{k}=0)/(2\pi)$ of the longitudinal optical phonons at the most pronounced structures in both materials

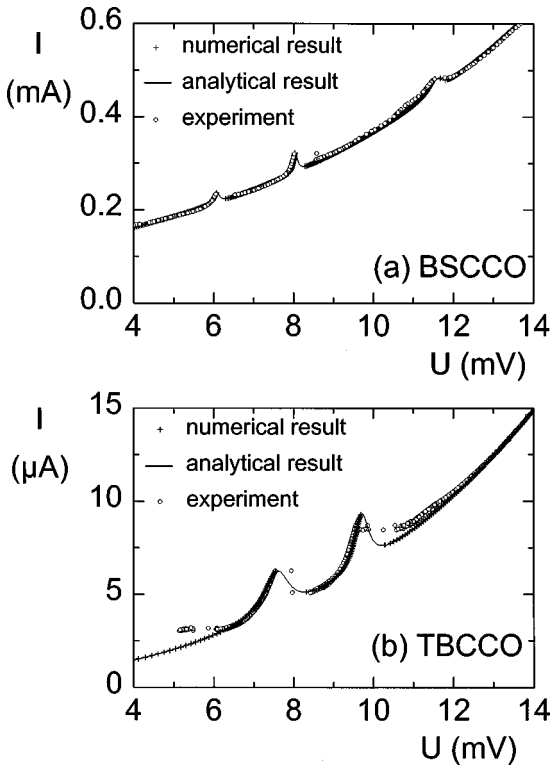

FIG. 27. Comparison between measured and numerically calculated I-V characteristic for BSCCO (a) and TBCCO (b). The parameter used for the simulation are (a) for BSCCO: $\beta_c = 800$, $\nu_{0,1} = 2.80$ THz, $S_1 = 1.35$, $r_1 = 0.08$ THz, $\nu_{0,2} = 3.62$ THz, $S_2 = 1.5$, $r_2 = 0.05$ THz, $\nu_{0,3} = 4.91$ THz, $S_3 = 1.65$, $r_3 = 0.2$ THz, $\epsilon_\infty = 7.5$; and (b) for TBCCO: $\beta_c = 375$, $\nu_{0,1} = 3.28$ THz, $S_1 = 2.87$, $r_1 = 0.4$ THz, $\nu_{0,2} = 4.45$ THz, $S_2 = 0.68$, $r_2 = 0.2$ THz, $\epsilon_\infty = 8.45$.

are $\nu_{\rm LO,1} = 3.65$ THz and $\nu_{\rm LO,2} = 4.70$ THz for TBCCO and $\nu_{\rm LO,1} = 2.96$ THz, $\nu_{\rm LO,2} = 3.90$ THz, and $\nu_{\rm LO,3} = 5.71$ THz for BSCCO (cf. Table III).

With the help of the analytical relations derived above, some special points of the I-V characteristic $I(V)$ near the subgap structures can be identified.

(i) For small voltages $\omega \ll \omega_0$, one gets $\epsilon(\omega) \approx \epsilon(0) = {\rm const}$ and the model reduces to the conventional RSJ model. For this it is well known[67] that at $V_{\rm min} \approx 4\omega_J/\pi$ there is a voltage jump to the zero voltage state.

(ii) At the resonance $\omega = \omega_0$ of the phononic oscillator, both the real and the imaginary part of $\tilde{\epsilon}$ are strongly enhanced and the I-V characteristic in Eq. (22) reduces to the quasiparticle term. This corresponds to a pure quasiparticle tunneling current across the junction, while the supercurrent and the displacement current are compensating each other (cf. Fig. 28).

(iii) In contrast to the latter, Eq. (22) indicates a resonance in $I(V)$ near the zeros of ϵ_1, i.e., the eigenfrequencies $\omega_{\rm LO}$ of *longitudinal* optical phonons (cf. Fig. 28). The difference $\Delta\omega := \omega_{\rm LO} - \omega_{\rm max}$ between $\omega_{\rm LO}$ and the actual maximum $\omega_{\rm max}$ of $I(V)$ is due to the quasiparticle and phonon damping and can be estimated as $\Delta\omega < 2\%$. Physically this voltage is connected with an oscillation of the electric field E and the polarization P with vanishing displacement current density $\dot{D}$.

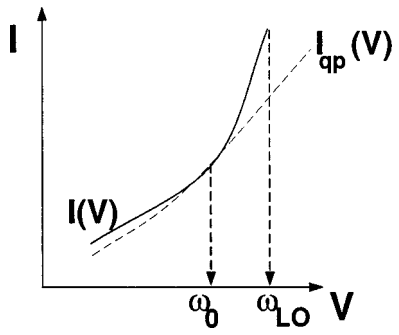

FIG. 28. Sketch of a quasiparticle I-V characteristic $I_{qp}(V)$, a structure in the total I-V characteristic $I(V)$, and the relevant phonon frequencies ω_0 and ω_{LO}.

With the help of Eq. (22), also an analytical formula for the intensity,

$$\Delta I_{\max} := \Delta I\left(\frac{\hbar}{2e}\omega_{LO}\right) = \frac{1}{2}\left(\frac{\omega_J}{\omega_{LO}}\right)^2 \frac{I_c}{\left(\epsilon_2(\omega_{LO}) + \frac{\sigma}{\epsilon_0\omega_{LO}}\right)}$$

$$= \frac{1}{2}\left(\frac{\omega_J}{\omega_{LO}}\right)^2 \frac{1}{\tilde{\epsilon}(\omega_{LO})} I_c, \qquad (26)$$

of the subgap structures can be derived. Thereby it turns out that a small damping parameter r, corresponding to a weak coupling of interlayer ions in neighboring contacts or equivalently the small dispersion of the phonons in the c direction, is crucial for the existence of a hysteretic region; no maximum of $I(V)$ can be found for $r \geqslant r_{crit} = \omega_{LO} - \omega_0$. Also note that the intensity is proportional to the critical current I_c, which is compatible with the experimental data presented in Sec. IV C.

In addition to this, the differential conductivity dI/dV can be derived, which is plotted in Fig. 29 together with the experimental result. Note that there exists a region of negative differential conductivity for voltages V slightly larger than $(\hbar/2e)\omega_{LO}$, which cannot be reached in a current-biased experiment with a continously increasing (decreasing) bias current. The extrema of the differential resistivity at the subgap structures are the reasons for a significantly enhanced microwave emission at low frequencies near the maxima of the I-V characteristic, as reported in Sec. IV F.

Also the properties of the model under microwave irradiation (cf. Sec. IV G) have been investigated for external frequencies ω_{rf} small compared with the Josephson plasma frequency ($\omega_{rf} \ll \omega_J$). With the modified ansatz

$$\gamma(t) = \gamma_0 + \omega t + \gamma_1 \sin(\omega t) + \gamma_{rf} \sin(\omega_{rf} t + \phi), \qquad (27)$$

the I-V characteristic is given by

$$j(V) = j_{qp}(V) - \frac{1}{2} j_c \left(\frac{\omega_J}{\omega}\right)^2 J_0(\gamma_{rf}) \mathrm{Im}\left(\frac{1}{\tilde{\epsilon}(\omega)}\right). \qquad (28)$$

It is seen that the intensity of the structures decreases with increasing external rf fields due to the well-known reduction of the plasma frequency $\omega_{J,\mathrm{eff}}^2 = \omega_J^2 J_0(\gamma_{rf})$ or the critical current j_c, respectively. The splitting of each subgap resonance into two maxima on the I-V curve, as discussed in Sec. IV G,

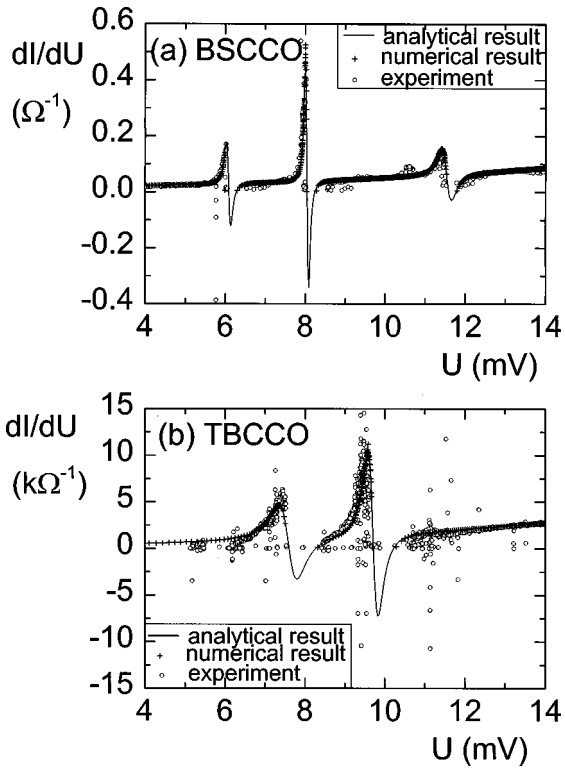

FIG. 29. Experimental (circles), numerical (crosses), and analytical results (solid line) for the differential conductivity of BSCCO (a) and TBCCO (b). The parameters used in the simulation are given in Fig. 27. The experimental data are calculated as differences between adjacent measured I-V data.

can be reproduced in a numerical simulation, which is shown in Fig. 30. Thereby the hysteresis of the subgap structures vanishes and the separation of the two maxima increases with increasing microwave power.

This extended RSJ model including the interaction of the oscillating current with infrared active optical c-axis phonons provides a simple and natural explanation for the subgap structures. There are at least two reasons why such an interaction was never before observed experimentally in other kinds of Josephson junctions. First, the intrinsic junctions are perfectly epitaxial layer by layer and therefore pro-

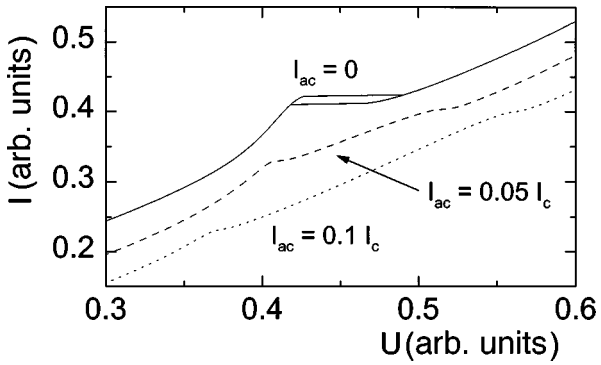

FIG. 30. Numerical simulation of the I-V characteristic with microwave irradiation. Solid curve shows the unperturbed I-V curve, dashed and dotted curves (shifted down for clarity) show I-V curves for different ac amplitudes (dashed, $I_{ac} = 0.05 I_c$; dotted, $I_{ac} = 0.1 I_c$).

vide the basis for well defined lattice vibrations. Second, there are weakly damped, infrared active phonons well below the gap in high-T_c superconductors. The model explains the independence of the voltage positions on temperature, magnetic field, geometry, and the number of resistive junctions as the phonon frequencies are insensitive to these quantities. It also explains the nearly constant value of the intensity in the temperature range up to $T=50$ K, where the critical current decreases only slightly. It should be emphasized that not all structures are necessarily caused by the same mechanism, i.e., a different mechanism for the appearence of some less pronounced structures is possible. The measured voltage position of the structures as listed in Table III for BSCCO allow us to determine the *precise* value of the longitudinal phonon frequencies ω_{LO}. The validity of the model can easily be checked with precise data for optical phonons. In fact, the relevant infrared active modes are expected and observed in the frequency range of the subgap structures.[74,75] However, the discrepancies between the different sources are considerably higher than the mutual deviation of our experimental data for all samples investigated.

The model can be generalized to a model describing a stack of Josephson junctions coupled due to phonons. Also, the additional coupling due to the effect recently proposed by Machida *et al.*[43] can be incorporated without any qualitative changes in the main results.[44]

V. CONCLUSIONS

The intrinsic stacks of Josephson junctions in $Bi_2Sr_2CaCu_2O_{8+\delta}$ and $Tl_2Ba_2Ca_2Cu_3O_{10+\delta}$ exhibit multiple branched I-V characteristics. By comparing the first branch, with a single junction in the resistive state, to branches of higher order, including more resistive junctions, we were able to show that all junctions have identical tunneling characteristics. At least to a good approximation the overall I-V characteristic in zero magnetic field can be described by the assumption of essentially independent junctions. The general curvature (without subgap structures) of the quasiparticle branch can be explained by a $d_{x^2-y^2}$-wave density of states for the superconductors in the CuO_2 planes and the standard tunneling formalism. The I_cR_n product of the intrinsic junctions was determined to be about 2–3 meV for both materials and is significantly smaller than predicted theoretically.

At voltages well below the gap, pronounced subgap structures were observed in the I-V characteristics of $Bi_2Sr_2CaCu_2O_{8+\delta}$ as well as $Tl_2Ba_2Ca_2Cu_3O_{10+\delta}$. The voltage positions of these structures are independent of temperature, sample geometry, magnetic field (directed either perpendicular or parallel to the layers), and independent of the number of junctions in the resistive state. In principle, the structures can be explained by subgap peaks in the density of states theoretically proposed for superconducting superlattices. However, the alternative explanation based on an interaction between infrared active optical c-axis phonons and Josephson ac currents would seem to provide a more natural explanation for the occurrence and behavior of at least the most pronounced structures. If the coupling between phonons and Josephson currents is indeed the mechanism responsible for the subgap structures, then the results presented in this paper would represent an experimental observation of a new high frequency effect in Josephson junctions. Furthermore, the provided data for these structures can help to determine phonon frequencies and oscillator strengths with high precision.

ACKNOWLEDGMENTS

The authors would like to thank L.N. Bulaevskii, U. Gunsenheimer, A. Hahn, S. Hofmann, J. Takeya, O. Waldmann, and A. Yurgens for valuable discussions, D. Pooke for providing some of the BSCCO crystals, and H. Kohlstedt for the Nb Josephson junction stack. This work has been supported by a grant of the Bayerische Forschungsstiftung within the research program FORSUPRA and by the Studienstiftung des Deutschen Volkes (C.H.).

*Present address: Department of Physics, University of California, and Material Sciences Division, Lawrence Berkeley National Laboratory, Berkeley, CA 94720.

[1] R. Kleiner, F. Steinmeyer, G. Kunkel, and P. Müller, Phys. Rev. Lett. **68**, 2394 (1992); R. Kleiner and P. Müller, Phys. Rev. B **49**, 1327 (1994).

[2] K. Schlenga, G. Hechtfischer, W. Walkenhorst, P. Müller, F.X. Régi, H. Savary, J. Schneck, M. Veith, W. Brodkorb, and E. Steinbeiß, IEEE Trans. Appl. Supercond. **5**, 3272 (1995).

[3] K. Schlenga, G. Hechtfischer, W. Walkenhorst, P. Müller, A. Murk, W. Prusseit, M. Veith, W. Brodkorb, and E. Steinbeiß, in *Proceedings of the 5th ISEC, Nagoya, Japan, 1995*, edited by H. Hayakawa (Institute of Physics, Bristol, 1996), p. 60.

[4] K. Schlenga, G. Hechtfischer, R. Kleiner, W. Walkenhorst, P. Müller, H. L. Johnson, M. Veith, W. Brodkorb, and E. Steinbeiß, Phys. Rev. Lett. **76**, 4943 (1996).

[5] K. Schlenga, G. Hechtfischer, R. Kleiner, W. Walkenhorst, P. Müller, and H.L. Johnson, Czech. J. Phys. **46**, Suppl. 3, 1277 (1996).

[6] M. Veith, T. Eick, W. Brodkorb, M. Manzel, H. Bruchlos, T. Köhler, H.-G. Schmidt, E. Steinbeiß, H.-J. Fuchs, K. Schlenga, G. Hechtfischer, and P. Müller, J. Appl. Phys. **80**, 3396 (1996).

[7] G. Hechtfischer, R. Kleiner, K. Schlenga, W. Walkenhorst, P. Müller, and H.L. Johnson, Phys. Rev. B **55**, 14 638 (1997).

[8] J.U. Lee, J.E. Nordman, and G. Hohenwarter, Appl. Phys. Lett. **67**, 1471 (1995); J.U. Lee, P. Guptasarma, D. Hornbaker, A. El-Kortas, D. Hinks, and K.E. Gray, *ibid.* **71**, 1412 (1997).

[9] H.L. Johnson, G. Hechtfischer, G. Götz, R. Kleiner, and P. Müller, J. Appl. Phys. **82**, 756 (1997).

[10] A. Yurgens, D. Winkler, N. Zavaritsky, and T. Claeson, Proc. SPIE **2697**, 433 (1996).

[11] A. Yurgens, D. Winkler, N.V. Zavaritsky, and T. Claeson, Phys. Rev. B **53**, 8887 (1996).

[12] P. Seidel, A. Pfuch, U. Hübner, F. Schmidl, H. Schneidewind, T. Ecke, and J. Scherbel, Physica C **293**, 49 (1997).

[13] J. Takeya, S. Akita, J. Shimoyama, and K. Kishio, Physica C **261**, 21 (1996).

[14] T. Yasuda, M. Tonouchi, and S. Takano, Czech. J. Phys. **46**, 1265 (1996).

[15] K. Tanabe, Y. Hidaka, S. Karimoto, and M. Suzuki, Phys. Rev. B **53**, 9348 (1996).

[16] Mikitaka Itoh, Shin-ichi Karimoto, Kazuichi Namekawa, and Mi-

noru Suzuki, Phys. Rev. B **55**, 12 001 (1997).
[17] Z.-X. Shen and D.S. Dessau, Phys. Rep **253**, 1 (1995).
[18] T.P. Devereaux, D. Einzel, B. Stadlober, R. Hackl, D.H. Leach, and J.J. Neumeier, Phys. Rev. Lett. **72**, 396 (1994); T.P. Devereaux, D. Einzel, B. Stadlober, and R. Hackl, *ibid.* **72**, 3291 (1994).
[19] O. Waldmann, F. Steinmeyer, Paul Müller, J.J. Neumeier, F.X. Régi, H. Savary, and J. Schneck, Phys. Rev. B **53**, 11 825 (1996).
[20] D.A. Wollman, D.J. van Harlingen, W.C. Lee, D.M. Ginsberg, and A.J. Leggett, Phys. Rev. Lett. **71**, 2134 (1993).
[21] D.J. van Harlingen, Rev. Mod. Phys. **67**, 515 (1995).
[22] C.C. Tsuei, J.R. Kirtley, C.C. Chi, L.S. Yu-Jahnes, A. Gupta, T. Shaw, J.Z. Sun, and M.B. Ketchen, Phys. Rev. Lett. **73**, 593 (1994); J.R. Kirtley, C.C. Tsuei, J.Z. Sun, C.C. Chi, L.S. Yu-Jahnes, A. Gupta, M. Rupp, and M.B. Ketchen, Nature (London) **373**, 225 (1995).
[23] T. van Duzer and C.W. Turner, *Principles of Superconductive Devices and Circuits* (Elsevier North Holland, New York, 1981).
[24] V. Ambegaokar and A. Baratoff, Phys. Rev. Lett. **10**, 486 (1963); **11**, 104(E) (1963).
[25] Y. Tanaka and S. Kashiwaya, Phys. Rev. B **56**, 892 (1997).
[26] Ivar Giaever, Phys. Rev. Lett. **5**, 147 (1960); **5**, 464 (1960).
[27] W.L. McMillan and J.M. Rowell, Phys. Rev. Lett. **4**, 108 (1965).
[28] Jin-Xiang Liu, Ji-Chun Wan, A.M. Goldman, Y.C. Chang, and P.Z. Jiang, Phys. Rev. Lett. **67**, 2195 (1991).
[29] E.L. Wolf, A. Chang, Z.Y. Rong, Yu. M. Ivanchenko, and F. Lu. J. Supercond. **7**, 355 (1994).
[30] Ch. Renner and Ø. Fischer, Phys. Rev. B **51**, 9208 (1995).
[31] M. Oda, C. Manabe, T. Abe, and M. Ido, Physica C **263**, 241 (1996).
[32] I. Takeuchi, J.S. Tsai, Y. Shimakawa, T. Manako, and Y. Kubo, Physica C **158**, 83 (1989).
[33] Qun Chen and K.-W. Ng, Phys. Rev. B **45**, 2569 (1992).
[34] Zhe Zhang and Charles M. Lieber, Phys. Rev. B **47**, 3423 (1993).
[35] Jin-Xiang Liu, S.W. Pierson, G.C. Spalding, Ji-Chun Wan, and A.M. Goldman, Europhys. Lett. **20**, 721 (1992).
[36] Jin-Xiang Liu, Stephen W. Pierson, G.C. Spalding, Ji-Chun Wan, and A.M. Goldman, Physica B **194-196**, 2233 (1994).
[37] H.J. Tao, A. Chang, Farun Lu, and E.L. Wolf, Phys. Rev. B **45**, 10 622 (1992).
[38] Hironaru Murakami, Shin-ichi Hiramatsu, and Ryozo Aoki, Physica C **261**, 302 (1996).
[39] R. Kleiner, M. Mößle, W. Walkenhorst, G. Hechtfischer, K. Schlenga, and Paul Müller, Physica C **282-287**, 2435 (1997).
[40] H.J. Tao, Farun Lu, G. Zhang, and E.L. Wolf, Physica C **224**, 117 (1994).
[41] S.I. Vedeneev, A.G.M. Jansen, and P. Wyder, Physica B **218**, 213 (1996).
[42] R. Kleiner, Phys. Rev. B **50**, 6919 (1994).
[43] M. Machida, T. Koyama, and M. Tachiki (unpublished); T. Koyama and M. Tachiki, Phys. Rev. B **54**, 16 183 (1996).
[44] Ch. Helm, Ch. Preis, and J. Keller (unpublished).
[45] N. Motohira, K. Kuwahara, T. Hasegawa, K. Kishio, and K. Kitazawa, J. Ceram. Soc. Jpn. **97**, 994 (1989).
[46] T. Stoto, D. Pooke, L. Forro, and K. Kishio (unpublished).
[47] M. Manzel, H. Bruchlos, G. Bruchlos, T. Eick, E. Steinbeiß, and L. Illgen, Phys. Status Solidi A **128**, 175 (1991); M. Manzel, H. Bruchlos, E. Steinbeiß, T. Eick, M. Klinger, J. Fuchs, and B. Kley, Physica C **201**, 337 (1992).
[48] S. Watanabe, H.S.J. van der Zant, S.H. Strogartz, and T.P. Orlando, Physica D **97**, 429 (1996).
[49] R. Kleiner, K. Schlenga, L.N. Bulaevski, and M.P. Maley (unpublished).
[50] D.E. McCumber, J. Appl. Phys. **39**, 3113 (1968).
[51] K.K. Likharev, *Dynamics of Josephson Junctions and Circuits* (Gordon and Breach Science Publishers, New York, 1986).
[52] D.R. Heslinga and T.M. Klapwijk, Phys. Rev. B **47**, 5157 (1993).
[53] H. Won and K. Maki, Phys. Rev. B **49**, 1397 (1994).
[54] I. Iguchi, Z. Wen, Phys. Rev. B **49**, 12 388 (1994).
[55] A.G. Sun, D.A. Gajewski, M.B. Maple, and R.C. Dynes, Phys. Rev. Lett. **72**, 2267 (1994).
[56] R. Kleiner, A.S. Katz, A.G. Sun, R. Summer, D.A. Gajewski, S.H. Han, S.I. Woods, E. Dantsker, B. Chen, K. Char, M.B. Maple, R.C. Dynes, and John Clarke, Phys. Rev. Lett. **76**, 2161 (1996).
[57] K.A. Kouznetsov, A.G. Sun, B. Chen, A.S. Katz, S.R. Bahcall, John Clarke, R.C. Dynes, D.A. Gajewski, S.H. Han, M.B. Maple, J. Giapintzakis, J.-T. Kim, and D.M. Ginsberg, Phys. Rev. Lett. **79**, 3050 (1997).
[58] J.H. Miller, Jr., Z.G. Zou, J.R. Liu, Z.S. Sheng, and W.K. Chu, Physica C **282-287**, 1515 (1997).
[59] G.E. Blonder, M. Tinkham, and T.M. Klapwijk, Phys. Rev. B **25**, 4515 (1982).
[60] L.C. Brunel, S.G. Louie, G. Martinez, S. Labdi, and H. Raffy, Phys. Rev. Lett. **66**, 1346 (1991).
[61] A.M. Rao, P.C. Eklund, G.W. Lehman, D.W. Face, G.L. Doll, G. Dresselhaus, and M.S. Dresselhaus, Phys. Rev. B **42**, 193 (1990).
[62] T.M. Klapwijk, G.E. Blonder, and M. Tinkham, Physica B & C **109&110**, 1657 (1982).
[63] J.R. Schrieffer and J.W. Wilkins, Phys. Rev. Lett. **10**, 17 (1963).
[64] N.R. Werthamer, Phys. Rev. **147**, 255 (1966).
[65] M. Fiske, Rev. Mod. Phys. **36**, 221 (1964).
[66] J.G. Chen, T.F. Finnegan, and D.N. Langenberg, Physica (Amsterdam) **55,** 413 (1971).
[67] A. Barone and G. Paterno, *Physics and Applications of the Josephson Effect* (Wiley, New York, 1982).
[68] R. Tsu and L. Esaki, Appl. Phys. Lett. **22**, 562 (1973).
[69] T.C.L.G. Sollner, W.D. Goodhue, P.E. Tennenwald, C.D. Parker, and D.D. Peck, Appl. Phys. Lett. **43**, 588 (1983).
[70] Ch. Helm, Ch. Preis, F. Forsthofer, J. Keller, K. Schlenga, R. Kleiner, and P. Müller, Physica C **293**, 60 (1997).
[71] A. Hahn, Physica B **165&166**, 1065 (1990); Sov. J. Low Temp. Phys. **18**, 447 (1992).
[72] H. Plehn, O.-J. Wacker, and R. Kümmel, Phys. Rev. B **49**, 12 140 (1994).
[73] Ch. Helm, Ch. Preis, F. Forsthofer, J. Keller, K. Schlenga, R. Kleiner, and P. Müller, Phys. Rev. Lett. **79**, 737 (1997).
[74] R.G. Buckley, M.P. Staines, D.M. Pooke, T. Stoto, and N.E. Flower, Physica C **248**, 247 (1995); J. Prade, A.D. Kulkarni, F.W. de Wette, U. Schröder, and W. Kress, Phys. Rev. B **39**, 2771 (1989).
[75] T. Zetterer, W. Ose, J. Schützmann, H.H. Otto, P.E. Obermeyer, N. Tasler, H. Lengfellner, G. Lugert, J. Keller, and K.F. Renk, J. Opt. Soc. Am. B **6**, 420 (1989); V.M. Burlakov, S.V. Shulga, J. Keller, and K.F. Renk, Physica C **203**, 68 (1992); M. Shimada, K. Mizuno, S. Miyamoto, M. Shimizu, and J. Tanaka, *ibid.* **193**, 353 (1992); B. Wallner, Ph.D. thesis, University of Regensburg, Germany, 1996.